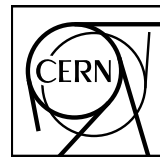


EUROPEAN ORGANIZATION FOR NUCLEAR RESEARCH



CERN-EP-2019 -XXX
Day Month 2019

ΛK femtoscopy in Pb-Pb collisions at $\sqrt{s_{\text{NN}}} = 2.76 \text{ TeV}$

ALICE Collaboration*

Abstract

We present the first measurement of the scattering parameters of ΛK pairs in all three charge combinations (ΛK^+ , ΛK^- , and ΛK_S^0). We achieve the measurements through our femtoscopic analysis of ΛK correlations in Pb-Pb collisions at $\sqrt{s_{\text{NN}}} = 2.76 \text{ TeV}$ from ALICE. The femtoscopic correlations result from strong final-state interactions, and are fit with a parametrization allowing us to both characterize the pair emission source and measure the scattering parameters for the particle pairs. We perform an extensive study with the THERMINATOR 2 event generator to account for both non-femtoscopic backgrounds, as well as contributions from residual correlations induced by feed-down from resonances. We find the non-femtoscopic background is due almost entirely to collective effects, and we are able to use the event generator to quantitatively describe it with unprecedented precision. In the experimental data, we observe a striking difference between the ΛK^+ and ΛK^- correlations in pairs with low relative momenta ($k^* \lesssim 100 \text{ MeV}$). The ΛK^+ system exhibits a negative real component of the scattering parameter ($\Re f_0$), while that of the ΛK^- is positive. The underlying cause dictating this interesting difference in the strong force between the two systems is not completely understood. The results might suggest an effect arising from different quark-antiquark interactions between the pairs ($s\bar{s}$ in ΛK^+ and $u\bar{u}$ in ΛK^-), or from different net strangeness for each system ($S=0$ for ΛK^+ , and $S=-2$ for ΛK^-). Finally, we find that the ΛK systems exhibit source radii larger than expected from extrapolation from identical particle femtoscopic studies. We understand this effect to result from the separation in space-time of the single-particle Λ and K source distributions.

© 2019 CERN for the benefit of the ALICE Collaboration.

Reproduction of this article or parts of it is allowed as specified in the CC-BY-4.0 license.

*See Appendix F for the list of collaboration members

24 1 Introduction

25 Femtoscopy is an experimental method used to study the space-time characteristic of the particle emitting
 26 sources in relativistic particle collisions [1]. With this method, two(or many)-particle relative-momentum
 27 correlation functions are used to connect the final-state momentum distributions to the space-time distri-
 28 butions of particle emission at freeze-out. The correlation functions are sensitive to quantum statistics, as
 29 well as strong and Coulomb final-state interactions (FSI). In addition to characterizing the source region,
 30 femtoscopy offers a unique opportunity to measure nuclear scattering parameters, many of which are
 31 difficult, if not impossible, to measure otherwise. In many pair systems, the contributions to the cor-
 32 relation function from quantum statistics and/or the Coulomb interaction overwhelm that of the strong
 33 interaction, making it difficult to extract scattering information. In this article, we study non-identical
 34 particle pairs, with at least one electrically neutral particle in the pair. Therefore, quantum statistics and
 35 the Coulomb interaction do not contribute, giving us a clear signal from the strong interaction.

36 Femtoscopic analyses of pion, kaons, and protons have revealed a trend of decreasing source radii with
 37 increasing transverse mass [2], which, for identical particle pairs, is defined as $m_T^2 = m^2 + k_T^2$, where
 38 $k_T = \frac{1}{2}|\mathbf{p}_{T,1} + \mathbf{p}_{T,2}|$. This is interpreted as a signature of hydrodynamic flow, and therefore deconfined
 39 quark matter, in the heavy-ion collisions [3]. The exponent for m_T -scaling can be shown analytically to
 40 be $-\frac{1}{2}$ for case of a one-dimensional longitudinal hydrodynamic expansion with negligible transverse
 41 flow and common freeze-out characteristics, regardless of particle species. This has lead to an idea
 42 of universal m_T -scaling for different particle species. However, it is unclear how picture changes with
 43 significant transverse flow, viscosity corrections, and hadronic rescattering. Additionally, the scaling
 44 observed in models exists separately for the three-dimensional radii in the Longitudinally Co-Moving
 45 System (LCMS), and will at best only be approximate in the Pair Rest Frame (PRF) [2, 4].

46 The radii we extract from our study are larger than one would expect from naively following the trends
 47 set forth in the identical particle analyses. However, when dealing with non-identical particles, such
 48 as in the present case with ΛK pairs, we should not necessarily expect the exact same trend. In such
 49 cases, the pair emission source, measured through femtoscopy, is the superposition of two single-particle
 50 sources, each with its own unique size, shape, and space-time position within the medium. Although the
 51 single-particle sources should abide by the approximate m_T -scaling, the pair sources generally will not.

52 This paper presents the first measurement of the scattering parameters of ΛK pairs in all three charge
 53 combinations (ΛK^+ , ΛK^- , and ΛK_S^0). The scattering parameters, along with pair emission source sizes,
 54 are extracted with a femtoscopic analysis of ΛK correlations in Pb-Pb collisions at $\sqrt{s_{NN}} = 2.76$ TeV
 55 from ALICE experiment at the LHC. These correlations result from strong final-state interactions, and
 56 are fit with a parametrization by Lednicky and Lyuboshitz [5]. We perform an extensive study with the
 57 THERMINATOR 2 event generator to account for both non-femtoscopic backgrounds, as well as contribu-
 58 tions from residual correlations induced by feed-down from resonances. We find the non-femtoscopic
 59 background is due almost entirely to collective effects, and we are able to use the event generator to
 60 quantitatively describe it with unprecedented precision. In the experimental data, we observe a striking
 61 difference between the ΛK^+ and ΛK^- correlations in pairs with low relative momenta ($k^* \lesssim 100$ MeV).
 62 The ΛK^+ system exhibits a negative real component of the scattering parameter ($\Re f_0$), while that of the
 63 ΛK^- is positive. The underlying cause dictating this interesting difference in the strong force between
 64 the two systems is not completely understood. The results might suggest an effect arising from differ-
 65 ent quark-antiquark interactions between the pairs ($s\bar{s}$ in ΛK^+ and $u\bar{u}$ in ΛK^-), or from different net
 66 strangeness for each system ($S = 0$ for ΛK^+ , and $S = -2$ for ΛK^-). Finally, we find that the ΛK systems
 67 exhibit source radii larger than expected from extrapolation from identical particle femtoscopic studies.
 68 We understand this effect to be result from the separation in space-time of the single-particle Λ and K
 69 distributions. For the study of ΛK pairs at mid-rapidity in Pb-Pb collisions, we expect a separation of the
 70 single-particle sources in the out direction. The effect of a non-zero shift in the source will naturally lead
 71 to larger measured radii.

- 72 Note, we expect and observe consistent results between a particle pair and its conjugate (ex. ΛK^+ and
 73 $\bar{\Lambda} K^-$); therefore, we group the two together as a single analysis by fitting them simultaneously with
 74 a shared parameter set, and will refer to the joined analysis simply by the pair name, excluding the
 75 conjugate. So, for instance, $\Lambda K_S^0 \oplus \bar{\Lambda} K_S^0$ is simply ΛK_S^0 , $\Lambda K^+ \oplus \bar{\Lambda} K^-$ is ΛK^+ , etc.
- 76 The organization of this paper is as follows. In Sec. 2 we discuss briefly our methods for selecting the
 77 data. In Sec. 3 we present our analysis technique. We introduce the two particle correlation function, as
 78 well as the theoretical models with which we fit. This section also includes descriptions of our handling
 79 of residual correlations, corrections accounting for finite track momentum resolution, treatment of the
 80 non-femtoscopic background, as well as a brief description of our estimation systematic uncertainties.
 81 Our results are presented in Sec. 4, and concluding remarks are given in Sec. 5.

82 2 Data Analysis

83 The dataset analyzed is from Pb-Pb collisions at $\sqrt{s_{NN}} = 2.76$ TeV at the LHC measured by the ALICE
 84 detector [6]. Approximately 40 million combined central, semi-central, and minimum bias events were
 85 analyzed. The events were classified according to their centrality determined using the measured ampli-
 86 tudes in the V0 detectors [7]. In order for an event to be included in the analysis, the z-position of the
 87 reconstructed event vertex must be within 10 cm of the center of the ALICE detector, and the event must
 88 contain at least one particle of each type from the pair of interest (ex. for ΛK_S^0 analysis, an accepted
 89 event must contain at least one Λ and at least one K_S^0).

90 Charged particle tracking was performed using the Time Projection Chamber (TPC) [8] and the Inner
 91 Tracking System [6]. The ITS allows for high spatial resolution in determining the primary (collision)
 92 vertex. The determination of the momenta of the tracks was performed using tracks reconstructed with
 93 the TPC only and constrained to the primary vertex. A minimum requirement on the number of recon-
 94 structed TPC clusters was imposed, the purpose of which is to ensure both the quality of the track and
 95 good p_T resolution at large momenta, as well as to remove fake tracks.

96 Particle identification (PID) for reconstructed tracks was carried out using both the TPC and Time-of-
 97 Flight (TOF) detector [9, 10] in the pseudorapidity range $|\eta| < 0.8$. For TPC PID, a parametrized
 98 Bethe-Bloch formula was used to calculate the specific energy loss $\langle dE/dx \rangle$ in the detector expected
 99 for a particle with a given mass and momentum. For TOF PID, the particle mass was used to calculate
 100 the expected time-of-flight as a function of track length and momentum. For each PID method, a value
 101 ($N\sigma$) was assigned to each track denoting the number of standard deviations between the measured track
 102 information and calculated values. This procedure was repeated for four “particle species hypotheses”
 103 - electron, pion, kaon, and proton-, and, for each hypothesis, a different $N\sigma$ value was obtained per
 104 detector.

105 2.1 K^\pm selection

106 The single-particle selection criteria used to select charged kaon candidates are summarized in Table 1.
 107 K^\pm track detection utilized both TPC and TOF detectors, and tracks within the range $0.14 < p_T < 1.5$
 108 GeV/c were accepted. As we are interested in primary particles originating from the primary vertex,
 109 to reduce the number of secondaries (for instance, charged particles produced in the detector material,
 110 particles from weak decays, etc.) in our sample, we established a maximum cut on the distance-of-
 111 closest-approach (DCA) of the track to the primary vertex. This restriction is realized by imposing a
 112 DCA cut in both the transverse and beam directions.

113 PID was performed using both the TPC and TOF detectors via the $N\sigma$ method. Additionally, we include
 114 methods to reduce the contamination in our K^\pm samples from electrons and pions. The specifics for these
 115 cuts are contained in Table 1.

K[±] selection	
Transverse momentum p_T	$0.14 < p_T < 1.5 \text{ GeV}/c$
$ \eta $	< 0.8
Transverse DCA to primary vertex	$< 2.4 \text{ cm}$
Longitudinal DCA to primary vertex	$< 3.0 \text{ cm}$
TPC and TOF N σ Cuts	
$p < 0.4 \text{ GeV}/c$	$N_{\sigma K, \text{TPC}} < 2$
$0.4 < p < 0.45 \text{ GeV}/c$	$N_{\sigma K, \text{TPC}} < 1$
$0.45 < p < 0.80 \text{ GeV}/c$	$N_{\sigma K, \text{TPC}} < 3$ $N_{\sigma K, \text{TOF}} < 2$
$0.80 < p < 1.0 \text{ GeV}/c$	$N_{\sigma K, \text{TPC}} < 3$ $N_{\sigma K, \text{TOF}} < 1.5$
$p > 1.0 \text{ GeV}/c$	$N_{\sigma K, \text{TPC}} < 3$ $N_{\sigma K, \text{TOF}} < 1$
Electron Rejection: Reject if all satisfied	$N_{\sigma e^-, \text{TPC}} < 3$ $N_{\sigma e^-, \text{TPC}} < N_{\sigma K^\pm, \text{TPC}}$ $N_{\sigma e^-, \text{TOF}} < N_{\sigma K^\pm, \text{TOF}}$
Pion Rejection: Reject if:	
	TOF and TPC available
$p < 0.65 \text{ GeV}/c$	$N_{\sigma \pi, \text{TPC}} < 3$ $N_{\sigma \pi, \text{TOF}} < 3$
	Only TPC available
	$p < 0.5 \text{ GeV}/c$
	$N_{\sigma \pi, \text{TPC}} < 3$
	$0.5 < p < 0.65 \text{ GeV}/c$
	$N_{\sigma \pi, \text{TPC}} < 2$
$0.65 < p < 1.5 \text{ GeV}/c$	$N_{\sigma \pi, \text{TPC}} < 5$ $N_{\sigma \pi, \text{TOF}} < 3$
$p > 1.5 \text{ GeV}/c$	$N_{\sigma \pi, \text{TPC}} < 5$ $N_{\sigma \pi, \text{TOF}} < 2$

Table 1: K[±] selection

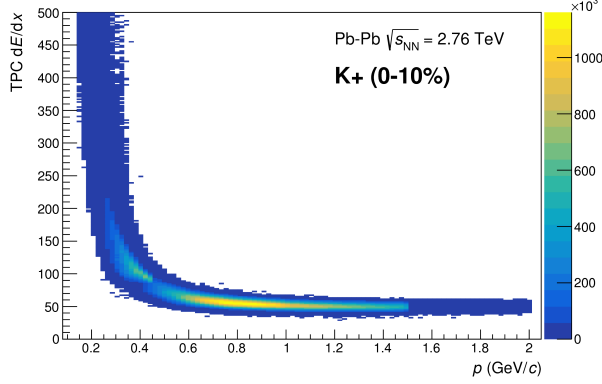


Fig. 1: Sample dE/dx distribution for the K^+ collection from our 0-10% central ΛK^+ analysis.

116 The purity of the K^\pm collections was estimated from a Monte-Carlo (MC) study based on HIJING [11]
 117 simulations using GEANT3 [12] to model particle transport through the ALICE detectors. In these
 118 simulations, the true identity of each reconstructed K^\pm particle is known; therefore, the purity may be
 119 estimated as:

$$\text{Purity}(K^\pm) = \frac{N_{\text{true}}}{N_{\text{reconstructed}}} \quad (1)$$

120 For our analysis, we find $\text{Purity}(K^+) \approx \text{Purity}(K^-) \approx 97\%$. Figure 1 shows a sample dE/dx for the K^+
 121 collection in the 0-10% centrality bin (from our ΛK^+ study).

122 2.2 V0 selection

123 $\Lambda(\bar{\Lambda})$ and K_S^0 particles are electrically neutral, and cannot be directly detected, but must instead be re-
 124 constructed through detection of their decay products, or daughters. This process is illustrated in Figure
 125 2, and the main cuts used are shown in Tables 2 and 3. In general, particles which are topologically
 126 reconstructed in this fashion are called V0 particles. The decay channel $\Lambda \rightarrow p\pi^-$ was used for the
 127 identification of Λ hyperons (and, similarly the charge-conjugate decay for the $\bar{\Lambda}$ identification), and K_S^0
 128 $\rightarrow \pi^+\pi^-$ for the identification of K_S^0 mesons.

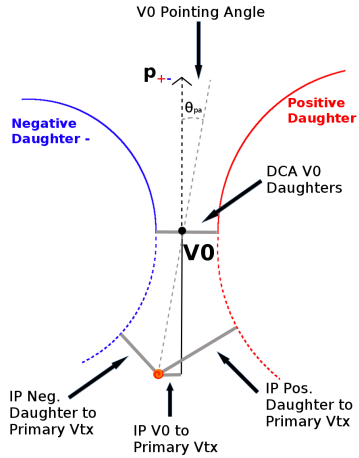


Fig. 2: V0 Reconstruction

129 To construct a V0 particle, the charged daughter tracks must first be found. Aside from typical kinematic
 130 and PID cuts (using TPC and TOF detectors), the daughter tracks are also exposed to a minimum cut

on their impact parameter with respect to the primary vertex. The daughters of a V0 particle should not originate from the primary vertex, but rather from the decay vertex of the V0, hence the minimum cut imposition. The decay vertex of the V0 is assumed to be the point of closest approach between the daughter tracks. To help ensure quality, a maximum value cut is demanded on the distance-of-closest-approach between the daughters (DCA V0 Daughters). The positive and negative daughter tracks are combined to form the V0 candidate, the momentum of which is simply the sum of the momenta of the daughters (calculated at the DCA).

A minimum transverse momentum cut on the V0 candidate is introduced to reduce contamination from fake candidates. Opposite to that of the daughter tracks, the V0 candidate is exposed to a maximum cut on its impact parameter with respect to the primary vertex. In this case, we do want our V0 candidates to be primary, hence the maximum cut imposition. To further strengthen our selection of primary V0 candidates, we impose a selection on the pointing angle, θ_{pa} , between the V0 momentum and the vector pointing from the primary vertex to the secondary V0 decay vertex. We want the V0 candidate's momentum to point back to the primary decay vertex, and therefore a small θ_{pa} ; we achieve this by appointing a minimum value on $\cos(\theta_{\text{pa}})$ (“Cosine of pointing angle” in Tables 2 and 3).

On occasion, $\Lambda(\bar{\Lambda})$ particles are misidentified as K_S^0 , and vice versa. To attempt to remove these contaminations without throwing away good candidates, we impose a set of misidentification cuts. The intent of these cuts is to judge whether a candidate is more likely a $\Lambda(\bar{\Lambda})$ or a K_S^0 , and are implemented as described below. For a given V0, we calculate the mass assuming different identities (Λ , $\bar{\Lambda}$, K_S^0) of the candidate; the mass assuming K_S^0 hypothesis ($m_{\text{inv}, K_S^0 \text{ hyp.}}$) is calculated assuming $\pi^+\pi^-$ daughters, the mass assuming Λ hypothesis ($m_{\text{inv}, \Lambda \text{ hyp.}}$) is calculated assuming $p\pi^-$ daughters, and the mass assuming $\bar{\Lambda}$ hypothesis ($m_{\text{inv}, \bar{\Lambda} \text{ hyp.}}$) is calculated assuming $\bar{p}\pi^+$ daughters. In addition to the notation just introduced, in the following, m_{PDG, K_S^0} and $m_{\text{PDG}, \Lambda(\bar{\Lambda})}$ denote the particle masses of the K_S^0 and $\Lambda(\bar{\Lambda})$, respectively, as recorded by the Particle Data Group [13].

For $\Lambda(\bar{\Lambda})$ selection, a candidate is assumed to be misidentified and is rejected if all of the following criteria are satisfied:

$$1. \left| m_{\text{inv}, K_S^0 \text{ hyp.}} - m_{\text{PDG}, K_S^0} \right| < 9.0 \text{ MeV}/c^2$$

2. The daughter particles pass daughter cuts intended for K_S^0 reconstruction

(a) Λ selection

- i. p daughter passes π^+ cuts intended for K_S^0 reconstruction
- ii. π^- daughter passes π^- cuts intended for K_S^0 reconstruction.

(b) $\bar{\Lambda}$ selection

- i. π^+ daughter passes π^+ cuts intended for K_S^0 reconstruction
- ii. \bar{p} daughter passes π^- cuts intended for K_S^0 reconstruction.

$$3. \left| m_{\text{inv}, K_S^0 \text{ hyp.}} - m_{\text{PDG}, K_S^0} \right| < \left| m_{\text{inv}, \Lambda(\bar{\Lambda}) \text{ hyp.}} - m_{\text{PDG}, \Lambda(\bar{\Lambda})} \right|$$

Similarly, for K_S^0 selection, a candidate is rejected if all of the following criteria are satisfied for the Λ case, or for the $\bar{\Lambda}$ case:

$$1. \left| m_{\text{inv}, \Lambda(\bar{\Lambda}) \text{ hyp.}} - m_{\text{PDG}, \Lambda(\bar{\Lambda})} \right| < 9.0 \text{ MeV}/c^2$$

2. The daughter particles pass daughter cuts intended for $\Lambda(\bar{\Lambda})$ reconstruction

- 170 (a) π^+ daughter passes $p(\pi^+)$ daughter cut intended for $\Lambda(\bar{\Lambda})$ reconstruction
 171 (b) π^- daughter passes $\pi^-(\bar{p})$

172 3. $|m_{\text{inv}, \Lambda(\bar{\Lambda}) \text{ hyp.}} - m_{\text{PDG}, \Lambda(\bar{\Lambda})}| < |m_{\text{inv}, K_S^0 \text{ hyp.}} - m_{\text{PDG}, K_S^0}|$

173 At this stage, we have a collection of V0 candidates satisfying all of the aforementioned cuts. However,
 174 this collection is still polluted by fake V0s, for which the daughter particles happen to pass all of our cuts,
 175 but which do not actually originate from a V0. Although the two daughter particles appear to reconstruct
 176 a V0 candidate, they are lacking one critical requirement: the system invariant mass does not match that
 177 of our desired V0 species (these can be seen outside of the mass peaks in Fig. 3). Therefore, as our final
 178 single-particle cut, we require the invariant mass of the V0 candidate to fall within the mass peak of our
 179 desired species. Note, however, that some fake V0s still make it past this final cut, as their invariant mass
 180 also happens to fall without our acceptance window.

Λ selection	
Transverse momentum p_T	$> 0.4 \text{ GeV}/c$
$ \eta $	< 0.8
$ m_{\text{inv}} - m_{\text{PDG}} $	$< 3.8 \text{ MeV}$
DCA to primary vertex	$< 0.5 \text{ cm}$
Cosine of pointing angle	> 0.9993
Decay Length	$< 60 \text{ cm}$
Daughter Cuts (π and p)	
$ \eta $	< 0.8
DCA πp Daughters	$< 0.4 \text{ cm}$
π-specific cuts	
p_T	$> 0.16 \text{ GeV}/c$
DCA to primary vertex	$> 0.3 \text{ cm}$
TPC and TOF $N\sigma$ Cuts	
$p < 0.5 \text{ GeV}/c$	$N\sigma_{\text{TPC}} < 3$
$p > 0.5 \text{ GeV}/c$	$N\sigma_{\text{TPC}} < 3$
	$N\sigma_{\text{TOF}} < 3$
TOF & TPC available	$N\sigma_{\text{TPC}} < 3$
Only TPC available	$N\sigma_{\text{TPC}} < 3$
p-specific cuts	
p_T	$> 0.5(p) [0.3(\bar{p})] \text{ GeV}/c$
DCA to primary vertex	$> 0.1 \text{ cm}$
TPC and TOF $N\sigma$ Cuts	
$p < 0.8 \text{ GeV}/c$	$N\sigma_{\text{TPC}} < 3$
$p > 0.8 \text{ GeV}/c$	$N\sigma_{\text{TPC}} < 3$
	$N\sigma_{\text{TOF}} < 3$
TOF & TPC available	$N\sigma_{\text{TPC}} < 3$
Only TPC available	$N\sigma_{\text{TPC}} < 3$

Table 2: Λ selection

181 Occasionally, we encounter a situation where two V0 candidates share a common daughter. Not both of
 182 these candidates can be real V0s, and including both could introduce an artificial signal into our data.
 183 To avoid any auto-correlation effects, for each event, we impose a single-particle shared daughter cut on
 184 each collection of V0 candidates. This cut iterates through the V0 collection to ensure that no daughter is
 185 claimed by more than one V0 candidate. If a shared daughter is found between two V0 candidates, that
 186 candidate with a smaller DCA to primary vertex is kept while the other is excluded from the analysis.
 187 Note, this single-particle shared daughter cut is unique from the pair shared daughter cut discussed in
 188 Sec. 2.3, the latter of which ensure there is no daughter sharing between the particles in a given pair.

K_S^0 selection					
Transverse momentum p_T	$> 0.2 \text{ GeV}/c$				
$ \eta $	< 0.8				
$m_{PDG} - 13.677 \text{ MeV} < m_{\text{inv}} < m_{PDG} + 2.0323 \text{ MeV}$					
DCA to primary vertex	$< 0.3 \text{ cm}$				
Cosine of pointing angle	> 0.9993				
Decay Length	$< 30 \text{ cm}$				
π^\pm Daughter Cuts					
p_T	$> 0.15 \text{ GeV}/c$				
$ \eta $	< 0.8				
DCA $\pi^+ \pi^-$ Daughters	$< 0.3 \text{ cm}$				
DCA to primary vertex	$> 0.3 \text{ cm}$				
TPC and TOF $N\sigma$ Cuts					
$p < 0.5 \text{ GeV}/c$	$N\sigma_{\text{TPC}} < 3$				
$p > 0.5 \text{ GeV}/c$	<table border="1"> <tr> <td>TOF & TPC available</td><td>$N\sigma_{\text{TPC}} < 3$</td></tr> <tr> <td>Only TPC available</td><td>$N\sigma_{\text{TOF}} < 3$</td></tr> </table>	TOF & TPC available	$N\sigma_{\text{TPC}} < 3$	Only TPC available	$N\sigma_{\text{TOF}} < 3$
TOF & TPC available	$N\sigma_{\text{TPC}} < 3$				
Only TPC available	$N\sigma_{\text{TOF}} < 3$				
	$N\sigma_{\text{TPC}} < 3$				

Table 3: K_S^0 selection

189 In order to obtain a true and reliable signal, one must ensure good purity of the V0 collection. The purity
 190 of the collection is calculated as:

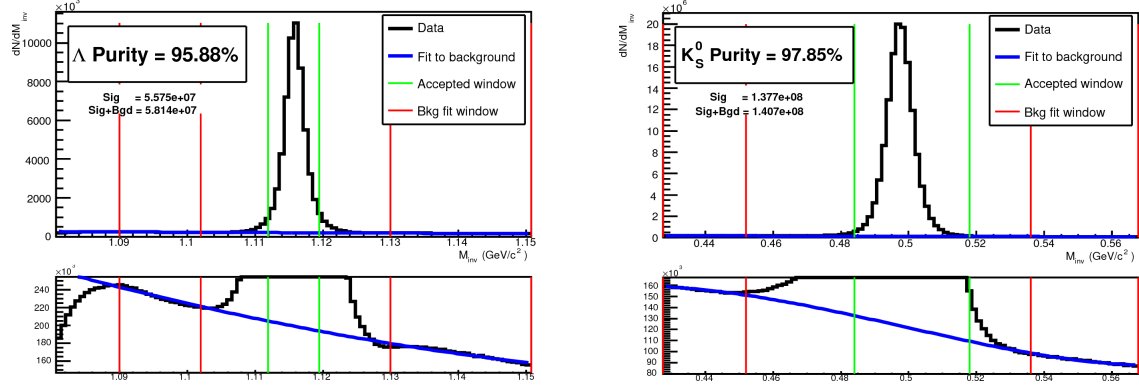
$$\text{Purity} = \frac{\text{Signal}}{\text{Signal} + \text{Background}} \quad (2)$$

191 To access both the signal and background, the invariant mass distribution (m_{inv}) of all V0 candidates
 192 must be constructed immediately before the final invariant mass cut, as shown in Fig. 3 for Λ and K_S^0
 193 candidates in the 0-10% centrality bin. Figure 3(a) presents the $p\pi^-$ invariant mass distribution showing
 194 the Λ peak, and Figure 3(b) presents the $\pi^+ \pi^-$ invariant mass distribution showing the K_S^0 peak. It is
 195 vital that this distribution be constructed immediately before the final m_{inv} cut, otherwise it would be
 196 impossible to estimate the background. These distributions (and similar for $\bar{\Lambda}$) are used to calculate the
 197 collections' purities (defined in Eq. 2). As shown in Figure 3, the background is fit (with a polynomial)
 198 outside of the peak region of interest to obtain an estimate for the background within the region. Within
 199 the m_{inv} cut limits, the background is assumed to be the region below the fit while the signal is that above
 200 the fit. The Λ and $\bar{\Lambda}$ purities were found to be $\approx 95\%$, and the K_S^0 purity was found to be $\approx 98\%$.

201 2.3 Pair Construction

202 The femtoscopic analysis of two-particle correlation functions relies on the proper formation of particle
 203 pairs. As such, it is important to obtain true particle pairs in the analysis. In particular, contamination
 204 from pairs constructed with split or merged tracks, and pairs sharing daughters, can introduce artificial
 205 signals into the correlation function, obscuring the actual physics. In an effort to remove contamination,
 206 we impose two main pair cuts: a shared daughter cut, and an average separation cut.

207 The purpose of the shared daughter cut is to ensure the first particle in the pair is unique from the second.
 208 For pairs formed of two V0s (i.e. ΛK_S^0), this cut is implemented by removing all pairs which share a
 209 daughter (ex. in ΛK_S^0 analysis, if the Λ and K_S^0 in a potential pair claim the same π^- daughter, the pair
 210 is excluded from the analysis). For a pair formed of a single V0 and a charged track (i.e. ΛK^\pm), the cut
 211 removes all pairs in which the charged track is also claimed as a daughter of the V0. This mistake could
 212 only occur if, for instance, either a K^\pm is misidentified as a π or p in the V0 reconstruction, or a π or p is
 213 misidentified as a K^\pm in the K^\pm selection.



(a) $p\pi^+$ invariant mass distribution where the Λ peak is seen. (b) $\pi^+\pi^-$ invariant mass distribution where the K_S^0 peak is seen.

Fig. 3: Invariant mass (m_{inv}) distribution of $p\pi^+$ pairs showing the Λ peak 3(a), and of $\pi^+\pi^-$ pairs showing the K_S^0 peak 3(b), for V0 candidates immediately before the final invariant mass cut (for the 0-10% centrality bin). The bottom panels are zoomed to show the background with fit. The vertical green lines represent the m_{inv} cuts used in the analyses, the red vertical lines delineate the region over which the background was fit, and the blue line shows the background fit. These distributions (and similar, for $\bar{\Lambda}$) are used to calculate the collection purities, $\text{Purity}(\Lambda) \approx \text{Purity}(\bar{\Lambda}) \approx 95\%$, and $\text{Purity}(K_S^0) \approx 98\%$.

214 The purpose of the average separation cut is to remove splitting and merging effects, and it is employed
 215 in the following way. To calculate the average separation between two tracks, the spatial separation is
 216 determined at several points throughout the TPC (every 20 cm radially from 85 cm to 245 cm), and the
 217 results averaged. For that ΛK_S^0 analysis, which involves two V0 particles, a minimum average separation
 218 cut of 6 cm between the like-charge daughters in the pairs was imposed (for example, between the p
 219 daughter of the Λ and the π^+ daughter of the K_S^0). For the ΛK^\pm analyses, a minimum average separation
 220 cut of 8 cm was enforced between the K^\pm and the Λ daughter sharing the same charge (for example, in the
 221 ΛK^+ analysis, between the p daughter of the Λ and the K^+). The values used in these cuts were obtained
 222 by first forming average separation correlation functions. This is done just as for our relative-momentum
 223 correlation functions, but we instead bin in average separation. Looking at these average separation
 224 correlation functions for like-charge tracks, at lowest average separation we see an enhancement due to
 225 track splitting, followed by (at slightly higher average separation) a suppression due to track merging.
 226 When the average separation correlation function stabilizes to unity, these effects are no longer abundant,
 227 and we choose our cut value. Splitting and merging effects between oppositely charged tracks was found
 228 to be negligible, therefore no cuts on unlike-charge tracks were imposed.

229 3 Analysis Methods

230 3.1 Correlation Function

231 Two-particle correlation functions are built as the ratio of the covariant two-particle and single-particle
 232 spectra:

$$C^{ab}(\vec{p}_a, \vec{p}_b) = \frac{E_a E_b \frac{dN^{ab}}{d^3 p_a d^3 p_b}}{(E_a \frac{dN^a}{d^3 p_a})(E_b \frac{dN^b}{d^3 p_b})} \quad (3)$$

233 This may be expressed theoretically as in the Koonin-Pratt equation [14, 15]:

$$C(\mathbf{k}^*) = \int S_{\mathbf{P}}(\mathbf{r}^*) |\Psi_{\mathbf{k}^*}(\mathbf{r}^*)|^2 d^3\mathbf{r}^* \quad (4)$$

234 where \mathbf{k}^* and \mathbf{r}^* are the relative momentum and separation in the pair rest frame, \mathbf{P} is the total pair
 235 momentum, $S_{\mathbf{P}}(\mathbf{r}^*)$ is the pair source distribution, and $\Psi_{\mathbf{k}^*}(\mathbf{r}^*)$ is the two-particle wave-function. Within
 236 the $|\Psi|^2$ term is contained the particle interaction information, and therefore the scattering parameters.
 237 Equation 4 reveals the limitations of femtoscopy; at best, we are able to probe the distribution of relative
 238 positions of particles with identical velocities and total momentum \mathbf{P} as they move in an asymptotic state.
 239 Therefore, we do not measure the entire size of the source, but rather the “regions of homogeneity” [3].

240 In practice, the correlation function is formed experimentally as:

$$C(k^*) = \mathcal{N} \frac{A(k^*)}{B(k^*)} \quad (5)$$

241 where $A(k^*)$ is the signal distribution, $B(k^*)$ is the reference distribution, and \mathcal{N} is a normalization
 242 parameter. $B(k^*)$ is used to divide out the phase-space effects, leaving only the femtoscopic effects in the
 243 correlation function. The normalization parameter is chosen such that the mean value of the correlation
 244 function equal unity for $k^* \in [0.32, 0.4] \text{ GeV}/c$.

245 In practice, $A(k^*)$ is constructed by binning in k^* pairs from the same event. Ideally, $B(k^*)$ is similar to
 246 $A(k^*)$ in all respects excluding the presence of femtoscopic correlations [1]. Typically, $B(k^*)$ is obtained
 247 by forming mixed-event pairs, i.e. particles from a given event are paired with particles from N_{mix}
 248 other events, and these pairs are then binned in k^* . Other techniques exist; most notably, one may use
 249 same-event pairs after rotating one particle in the pair by 180° in the transverse plane (see Sec. 3.5
 250 and App. B for more details). However, for this analysis, we use the typical mixed-event method. In
 251 forming the reference distribution, it is important to mix only similar events; mixing events with different
 252 phase-spaces can result in an unreliable reference, and can introduce artificial signals in the correlation
 253 function. Therefore, in this analysis, we bin our events both in primary vertex location (2 cm bin width)
 254 and in centrality (5% bin width), and we only mix events within a given bin; i.e. we only mix events
 255 of like centrality and of like primary vertex location. Additionally, we use $N_{\text{mix}} = 5$ as the size of our
 256 mixing pool. Also note, a vertex correction is also applied to each event, which essentially recenters the
 257 the primary vertices to $z = 0$.

258 This analysis presents correlation functions for three centrality bins (0-10%, 10-30%, and 30-50%), and
 259 is currently pair transverse momentum ($k_T = \frac{1}{2} |\mathbf{p}_{T,1} + \mathbf{p}_{T,2}|$) integrated (i.e. not binned in k_T). The
 260 correlation functions are constructed separately for the two magnetic field configurations (++ and - -),
 261 and are combined using a weighted average:

$$C(k^*) = \frac{\sum_i w_i C_i(k^*)}{\sum_i w_i} \quad (6)$$

262 where the sum runs over the correlation functions to be combined, and the weight, w_i , is the number of
 263 numerator pairs in the normalization range for $C_i(k^*)$.

264 3.2 Modeling the correlation function

265 In the absence of the Coulomb interaction, the correlation function can be described analytically with a
 266 model derived by Lednický and Lyuboshitz [5]. Within the model, the (non-symmetrized) two-particle
 267 wave function is expressed as a superposition of a plane wave and diverging spherical wave:

$$\Psi^S(\mathbf{k}^*, \mathbf{r}^*) = e^{-i\mathbf{k}^* \cdot \mathbf{r}^*} + f^S(k^*) \frac{e^{ik^* r^*}}{r^*} \quad (7)$$

268 In the effective range approximation, the complex s-wave scattering amplitude, $f^S(k^*)$, with S denoting
 269 the total spin of the particular pair, is of the form

$$f^S(k^*) = \left(\frac{1}{f_0^S} + \frac{1}{2} d_0^S k^{*2} - ik^* \right)^{-1} \quad (8)$$

270 where f_0^S is the complex s-wave scattering length, and d_0^S is the effective range of the interaction. A
 271 spherically symmetric Gaussian distribution is assumed for the pair emission source in the PRF

$$S(\mathbf{r}^*) \propto \exp \left[-\frac{r^{*2}}{4R_{\text{inv}}^2} \right] \quad (9)$$

272 where R_{inv} is the size of the source.

273 Assuming unpolarized emission, using the appropriately symmetrized form of Ψ (Eq. 7) with a spheri-
 274 cally symmetric Gaussian source (Eq. 9), with the Koonin-Pratt equation (Eq. 4), the correlation function
 275 for uncharged particles is given by [5]

$$C(k^*) = 1 + C_{\text{QI}}(k^*) + C_{\text{FSI}}(k^*) \quad (10)$$

276 C_{QI} describes plane-wave quantum interference:

$$C_{\text{QI}}(k^*) = \alpha \exp(-4k^{*2}R^2) \quad (11)$$

277 where $\alpha = (-1)^{2j}/(2j+1)$ for identical particles with spin j , and $\alpha = 0$ for non-identical particles. C_{FSI}
 278 describes the s-wave strong final state interaction between the particles:

$$C_{\text{FSI}}(k^*) = \sum_S \rho_S \left[\frac{1}{2} \left| \frac{f^S(k^*)}{R_{\text{inv}}} \right|^2 \left(1 - \frac{d_0^S}{2\sqrt{\pi}R_{\text{inv}}} \right) + \frac{2\Re f^S(k^*)}{\sqrt{\pi}R_{\text{inv}}} F_1(2k^* R_{\text{inv}}) - \frac{\Im f^S(k^*)}{R_{\text{inv}}} F_2(2k^* R_{\text{inv}}) \right] \quad (12)$$

279 where

$$F_1(z) = \int_0^z \frac{e^{x^2-z^2}}{z} dx; \quad F_2(z) = \frac{1-e^{-z^2}}{z} \quad (13)$$

280 The weight factor, ρ_S is the normalized emission probability for a state of total spin S ; in the assumed
 281 case of unpolarized emission, $\rho_S = (2S+1)/[(2j_1+1)(2j_2+1)]$, where $j_{1,2}$ are the spins of the particles
 282 in the pair.

283 An additional parameter λ is typically included in the femtoscopic fit function to account for the purity of
 284 the pair sample, as well as the presence of any uncorrelated pairs. In the case of no residual correlations
 285 (to be discussed in Section 3.3), the fit function becomes:

$$C(k^*) = 1 + \lambda [C_{\text{QI}}(k^*) + C_{\text{FSI}}(k^*)] \quad (14)$$

286 The presented formalism simplifies for the ΛK system. The particles in the pairs are obviously non-
 287 identical, therefore $\alpha = 0$, and we need not worry about the quantum statistical term, C_{QI} . Furthermore,
 288 Λ is spin-0 and K are spin-1/2, so the ΛK system only has one possible total spin state S , and therefore
 289 C_{FSI} has only a single term. In the following, we drop the S superscript from all scattering parameters.

290 **3.3 Residual Correlations**

291 The purpose of this analysis is study the interaction and scale of the emitting source of the primary ΛK
 292 pairs. In order to obtain correct results, it is desirable for our particle collections to consist of primary
 293 particles. In practice, this is impossible to achieve; many of our particles are not primary, but origi-
 294 nate as decay products from other resonances. Some of our Λ hyperons decay from Σ^0 , Ξ^0 , Ξ^- and
 295 $\Sigma^{*(+,-,0)}(1385)$ parents, and some of our K mesons decay from $K^{*(+,-,0)}(892)$ parents. In these decays,
 296 the daughter carries away a momentum very similar to that of its parent. As a result, the correlations be-
 297 tween the particles in the daughter pair will be sensitive to, and dependent upon, the interaction between
 298 the parents. In effect, the correlation between the parents will be visible, although smeared out, in the
 299 daughters' signal. We call this a residual correlation resulting from feed-down. Residual correlations
 300 are important in an analysis when three criteria are met [16]: i) the parent correlation signal is large,
 301 ii) a large fraction of pairs in the sample originate from the particular parent system, and iii) the decay
 302 momenta are comparable to the expected correlation width in k^* .

303 As it is difficult for us to eliminate these residual correlations in our analyses, we must attempt to account
 304 for them in our fit. The genuine ΛK correlation function may be combined with the contributions from
 305 residual feed-down and misidentified particles to obtain the final, measured correlation function:

$$C_{\text{measured}}(k_{\Lambda K}^*) = 1 + \lambda'_{\Lambda K}[C_{\Lambda K}(k_{\Lambda K}^*) - 1] + \sum_{i,j} \lambda'_{ij}[C_{ij}(k_{\Lambda K}^*) - 1] \quad (15)$$

$$\begin{aligned} \lambda'_{ij} &= \lambda_{\text{Fit}} \lambda_{ij} \\ \sum_{i,j} \lambda'_{ij} &= \lambda_{\text{Fit}} \sum_{i,j} \lambda_{ij} = \lambda_{\text{Fit}} \end{aligned}$$

306 where the ΛK term represents the genuine ΛK correlation, and the i, j terms denote the contributions
 307 from residual feed-down and possible impurities. More specifically, $C_{ij}(k_{\Lambda K}^*)$ is the correlation function
 308 between parents of particle species i and j , expressed in the basis of the relative momentum of the
 309 observed daughter ΛK pairs. The λ parameters serve as weight dictating the strength of the parent
 310 contribution to the daughter pair, and are normalized to unity. The individual λ_{ij} are fixed (and whose
 311 values can be found in Table A.1), but the parameter λ_{Fit} is left free. The λ_{Fit} parameter serves as an
 312 overall normalization shared by all contributors.

313 In order to obtain the parent correlation function expressed in the relative momentum of the daughter
 314 pair, one must use a transform matrix. The transform matrix describes the decay kinematics of the parent
 315 system into the daughter, and maps the k^* of the parent pair onto that of the daughter. Using this matrix,
 316 the transformed residual correlation function can be obtained:

$$C_{ij}(k_{\Lambda K}^*) \equiv \frac{\sum_{k_{ij}^*} C_{ij}(k_{ij}^*) T(k_{ij}^*, k_{\Lambda K}^*)}{\sum_{k_{ij}^*} T(k_{ij}^*, k_{\Lambda K}^*)} \quad (16)$$

317 The transform matrix is generated with the THERMINATOR 2 [17] simulation. It is formed for a given
 318 parent pair, ij , by taking all ΛK pairs originating from ij , calculating the relative momentum of the

319 parents (k_{ij}^*) and daughters ($k_{\Lambda K}^*$), and filling a two-dimensional histogram with the values. The transform
 320 matrix is essentially an unnormalized probability distribution mapping the k^* of the parent pair to that of
 321 the daughter pair when one or both parents decay.

322 Femtoscopic analyses are sensitive to the pair emission structure at kinetic freeze-out. Therefore, in the
 323 eyes of femtoscopy, any particle born from a resonance decay before last rescattering is seen as primary.
 324 For our study, when including three residual contributors, we consider a particle to be primary if its
 325 parent has a proper decay length of $c\tau < 10$ fm. When including ten residual contributors, we must
 326 reduce this number to $c\tau < 4$ fm for consistency. Moving to ten contributors, we introduce feed-down
 327 from Σ^* and K^* resonances, with proper decay lengths of $c\tau \approx 5$ fm and $c\tau \approx 4$ fm, respectively. As
 328 these are considered non-primary for the case of ten contributors, so must any resonance with $c\tau > 4$ fm.

329 As previously stated, the λ parameters dictate the strength of the parent contribution to the daughter pair.
 330 Therefore, the λ parameter for parent system AB can be estimated as the total number of ΛK pairs in our
 331 experimental sample originating from AB (N_{AB}) divided by the total number of ΛK pairs (N_{Total}):

$$\lambda_{AB} = \frac{N_{AB}}{N_{Total}} \quad (17)$$

332 The particle yields can be estimated using THERMINATOR 2 simulation (N_{ij}^{THERM}), while the reconstruc-
 333 tion efficiencies (RE_{ij}) are estimated with MC HIJING data, which has been run through GEANT to
 334 simulate the detector response. Thus, the λ parameters are estimated as:

$$\lambda_{AB} = \frac{N_{AB}}{N_{Total}} = \frac{N_{AB}^{THERM} RE_{AB}^{HIJING}}{\sum_{ij} N_{ij}^{THERM} RE_{ij}^{HIJING}} \quad (18)$$

335 The λ values used can be found in Table A.1, for the case of both three and ten residual contributors. In
 336 the table, we also list the λ values used for “Other” and “Fakes”. The “Other” category contains pairs
 337 which are not primary, and which do not originate from the (3 or 10) residual pairs included in the fit. The
 338 “Fakes” category represents pairs that are mistakenly identified as ΛK. To estimate this λ_{Fakes} value, we
 339 assumed that the number of fake pairs was equal to the total number of pairs multiplied by the Λ purity
 340 (i.e. assuming perfect purity for the kaons); or, more simply, $\lambda_{Fakes} = 1.0 - \text{Purity}(\Lambda)$. For both of these
 341 contributors (“Other” and “Fakes”), we assume that these correlations average to unity, and therefore do
 342 not contribute to the final correlation function.

343 In practice, we model the correlation function of the parents (ex. $\Sigma^0 K^+$), and run the correlation func-
 344 tion through the appropriate transform matrix to determine the contribution to the daughter correlation
 345 function (ex. ΛK^+). In an ideal world, we would simply look up the parent interaction in some table,
 346 and input this into our model, and form the parent correlation function, C_{ij} . Unfortunately, the world
 347 in which we live is not perfect, such a table does not exist, and little is known about the interaction be-
 348 between the particles in the residual pairs of this study. Additionally, introducing a unique set of scattering
 349 parameters and radii for each residual system would introduce a large number of additional fit parame-
 350 ters, for which we do not have many constraints, and would cause our fitter to be too unconstrained and
 351 yield untrustworthy results. For this analysis, we assume all residual pairs have the same source size
 352 as the daughter pair. Furthermore, we assume Coulomb-neutral residual pairs share the same scattering
 353 parameters as the daughter pair. Therefore, for Coulomb-neutral pairs, such as $\Sigma^0 K$, and $\Xi^0 K$, $C_{ij}(k_{ij}^*)$
 354 is calculated from Eqn. 10, with the help of Eqn. 12; $C_{ij}(k_{\Lambda K}^*)$ is then obtained by transforming $C_{ij}(k_{ij}^*)$
 355 with Eq. 16, using the appropriate transform matrix.

356 For residual pairs affected by both the strong and Coulomb interactions, things are a bit more compli-
 357 cated. This is due to the fact that, for the case of both strong and Coulomb interaction, we no longer
 358 have a nice analytical form with which to fit. Generating a correlation function including both is also

time consuming, as described further in Appendix C. When modeling $\Xi^- K^\pm$ residual correlations, we use the experimental $\Xi^- K^\pm$ data; in this case, there is no need to make any assumptions about scattering parameters or source sizes. For the other cases, we assume the strong interaction is negligible, and generate the parent correlation assuming a Coulomb-only scenario (see Appendix C for more details). This approximation is well justified here as a Coulomb-only description of the system describes, reasonably well, the broad features of the correlation; the strong interaction is necessary for the fine details. However, as these correlations are run through a transform matrix, which largely flattens out and fine details, a Coulomb-only description should be sufficient. This is reinforced by the fact that we find consistent results between using the ΞK data and the Coulomb-only model of the ΞK data in our treatment of the residual contribution.

369 3.4 Momentum Resolution Corrections

Finite track momentum resolution causes the reconstructed momentum of a particle to smear around the true value. This, of course, also holds true for V0 particles. The effect is propagated up to the pairs of interest, which causes the reconstructed relative momentum (k_{Rec}^*) to differ from the true momentum (k_{True}^*). Smearing of the momentum typically will result in a suppression and broadening of the signal.

The effects of finite momentum resolution can be investigated using the MC data, for which both the true and reconstructed momenta are available. Information gained from looking at k_{Rec}^* vs k_{True}^* can be exploited to generate response matrices. A response matrix describes quantitatively how each k_{Rec}^* bin receives contributions from multiple k_{True}^* bins, and can be used to account for the effects of finite momentum resolution. With this approach, the resolution correction is applied on-the-fly during the fitting process by propagating the theoretical (fit) correlation function through the response matrix, according to:

$$C_{\text{fit}}(k_{\text{Rec}}^*) = \frac{\sum_{k_{\text{True}}^*} M_{k_{\text{Rec}}^*, k_{\text{True}}^*} C_{\text{fit}}(k_{\text{True}}^*)}{\sum_{k_{\text{True}}^*} M_{k_{\text{Rec}}^*, k_{\text{True}}^*}} \quad (19)$$

where $M_{k_{\text{Rec}}^*, k_{\text{True}}^*}$ is the response matrix, $C_{\text{fit}}(k_{\text{True}}^*)$ is the fit binned in k_{True}^* , and the denominator normalizes the result. Equation 19 describes that, for a given k_{Rec}^* bin, the observed value of $C(k_{\text{Rec}}^*)$ is a weighted average of all $C(k_{\text{True}}^*)$ values, where the weights are the normalized number of counts in the $[k_{\text{Rec}}^*, k_{\text{True}}^*]$ bin.

385 3.5 Non-Flat Background

We observe a significant non-femtoscopic, non-flat, background in all of our correlations at large k^* . This background increases with decreasing centrality, is the same amongst all ΛK^\pm pairs, and is more pronounced in the ΛK_S^0 system. This difference in ΛK^\pm and ΛK_S^0 backgrounds is due mainly to the difference in kinematic cuts, not due to any interesting physics.

It is suggested that this background effect is due primarily to particle collimation associated with elliptic flow [18]. More specifically, these backgrounds result from mixing events with unlike event-plane angles (Ψ_{EP}). As explained in [18], when elliptic flow is present, all particles are more likely to be emitted in a specific direction (in-plane), as opposed to a perpendicular direction. Therefore, the difference in momenta for pairs of particles tends to be smaller, compared to the case of no flow. In the case of mixed-event pairs, the two events used do not share an event-plane, and therefore there is no collimation effect in the pairs from flow. As a result, pairs with larger momentum are more likely when mixed-events are used (in the denominator of the correlation function), causing the correlation function to dip below unity. This same reasoning suggests that the background should lead to an enhancement at low- k^* .

399 The issue here is that we need to know the behavior of the non-femtoscopic background in the low-
 400 k^* region, but we only cleanly observe it in the region further out where there is no femtoscopic signal.
 401 Unfortunately, we cannot simply rotate each event to artificially align their event-planes and rid ourselves
 402 of this mixing effect, as our azimuthal angle acceptance is not perfectly uniform, and we have only finite
 403 event-plane resolution. With better resolution, one could simply bin events in Ψ_{EP} and only mix events
 404 within a given bin. We pursued this direction, and observed a slight decrease in the background; however,
 405 going to finer binning, we saw no additional reduction in the background, signaling that we had reached
 406 the limits dictated by the resolution. In the end, we are forced to model the background to include it into
 407 our fit.

408 THERMINATOR 2 simulation has been shown to reproduce the background features in a πK analysis
 409 [18]. After issuing each simulated event a random Ψ_{EP} , we found THERMINATOR 2 did an exceptional
 410 job of describing our data. Furthermore, the simulation showed the non-femtoscopic background affects
 411 the correlation function as a separable scale factor. Figure 4 shows the THERMINATOR 2 simulation
 412 (gold) together with experimental data (red, blue, or black). The figure also shows a 6th-order polynomial
 413 fit to the simulation (gold), as well as the fit polynomial scaled to match the data (red, blue, black).

414 The description by THERMINATOR 2 of the non-femtoscopic backgrounds in the ΛK^\pm systems is re-
 415 markable, and can be used in a quantitative fashion to help fit the data. More specifically, the non-
 416 femtoscopic backgrounds were modeled by (6th-)order polynomial fits to THERMINATOR 2 simulation
 417 for the ΛK^\pm analyses; one polynomial for each centrality class. The form of each polynomial was set
 418 before use with the experimental data, by fitting to the THERMINATOR 2 simulation, shown in Fig. 4.
 419 At the time of the fit, the polynomial used to correct each correlation function could only be adjust by a
 420 simple scale factor to best match the data.

421 The description of the ΛK_S^0 is good at a qualitative level, but not quantitatively good enough to be utilized
 422 in our fit. As such, we use a linear form to model the background in the ΛK_S^0 system. The background for
 423 each correlation function was fixed before use in the signal region by fitting a linear form to the region
 424 $0.6 < k^* < 0.9$ GeV/c. In all cases, the non-femtoscopic background correction was applied as a scale
 425 factor.

426 An alternative approach to treating the non-femtoscopic background is to instead attempt to eliminate
 427 it. The background may be effectively reduced by forming the reference distribution ($B(k^*)$) with the
 428 “Stavinskiy method”. With the Stavinskiy method, mixed-event pairs are not used for the reference
 429 distribution; instead, same-event pseudo-pairs, formed by rotating one particle in a real pair by 180°
 430 in the transverse plane, are used. This rotation rids the pairs of any femtoscopic correlation, while
 431 maintaining correlations due to elliptic flow (and other suitably symmetric contributors). The effect on
 432 our ΛK^+ correlation functions can be seen in the appendix, in Fig. B.1.

433 3.6 Summarized Fit Procedure

434 A simple χ^2 test is inappropriate for fitting correlation functions, as the ratio two Poisson distributions
 435 does not result in a Poisson distribution. Instead, a log-likelihood fit function of the following form is
 436 used [1]:

$$\chi_{PML}^2 = -2 \left[A \ln \left(\frac{C(A+B)}{A(C+1)} \right) + B \ln \left(\frac{A+B}{B(C+1)} \right) \right] \quad (20)$$

437 where A is the experimental signal distribution (numerator), B is the experimental reference distribution
 438 (denominator), and C is the theoretical fit correlation function. Therefore, we use Eq. 20 as the statistic
 439 quantifying the quality of the fit. The parameters of the fit are: λ , R , f_0 ($\Re f_0$ and $\Im f_0$ separately), d_0 ,
 440 and normalization N .

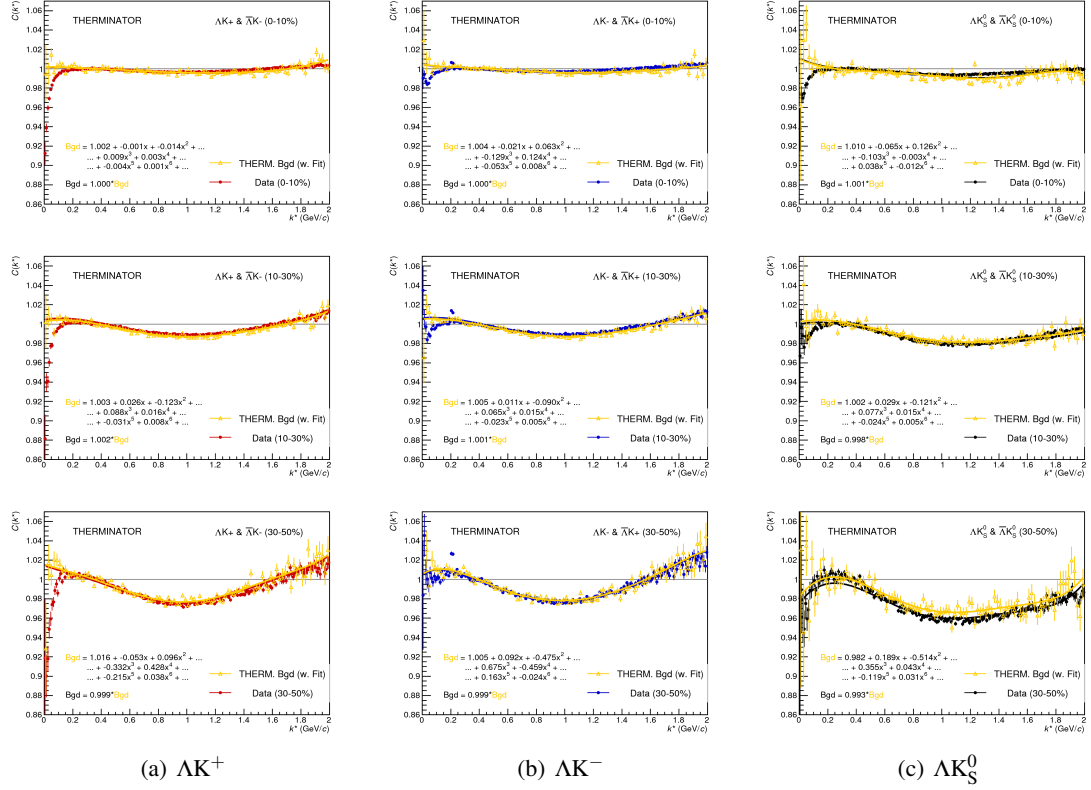


Fig. 4: THERMINATOR 2 simulation (gold) together with experimental data (red, blue, or black). The left column shows results for ΛK^+ (4(a)), middle for ΛK^- (4(b)), and right for ΛK_S^0 (4(c)). A 6th-order polynomial fit to the simulation is shown as a solid gold line, and whose fit parameters are printed on the lower left of each plot. This polynomial is scaled to match the experimental data; the value of this scale is printed in the lower left corner of each plot. The polynomial fit with scale factor applied is drawn in a color matching the experimental data (red, blue, black).

- 441 With our procedure, we are able to share parameters between different analyses and fit all simultaneously.
 442 A given pair and its conjugate (e.g. ΛK^+ and $\bar{\Lambda} K^-$) always share scattering parameters ($\Re f_0$, $\Im f_0$, d_0).
 443 However, the three distinct analyses (ΛK^+ , ΛK^- , and ΛK_S^0) are assumed to have scattering parameters
 444 unique from each other. We assume the pair emission source for a given centrality class is similar between
 445 all analyses; therefore, for each centrality, all ΛK analyses share a common radius parameter. We assume
 446 the same is true for the overall normalization λ parameters in Eq. 16. Finally, each correlation function
 447 has a unique normalization parameter.
- 448 All correlation functions were normalized in the range $0.32 < k^* < 0.40$ GeV/c, and fit in the range 0.0
 449 $< k^* < 0.30$ GeV/c. For the ΛK^- analysis, the region $0.19 < k^* < 0.23$ GeV/c was excluded from the
 450 fit to exclude the bump caused by the Ω^- resonance. For each pair system, we account for contributions
 451 from three residual contributors, as discussed in Sec. 3.3, and whose individual λ values are listed in
 452 Table A.1 (the cases of zero and ten residual contributors were also investigated, but the case of three
 453 contributors was deemed most reasonable). We account for effects of finite track momentum resolution,
 454 as outlined in Sec. 3.4. The non-femtoscopic backgrounds are modeled using the THERMINATOR 2
 455 simulation for the ΛK^\pm analyses, and with a linear form for the ΛK_S^0 system, as described in Sec. 3.5. In
 456 general, corrections are applied to the fit function, the raw data is never touched.
- 457 To summarize, the complete fit function is constructed as follows:

- 458 1. The uncorrected, primary, correlation function, $C_{\Lambda K}(k_{\text{True}}^*)$, is constructed using Eqns. 10 and 12

- 459 2. The correlation functions describing the parent systems which contribute residually are obtained
460 using:
 - 461 – Eqns. 10 and 12 for the case of Coulomb-neutral pairs
 - 462 – $\Xi^- K^\pm$ experimental data for $\Xi^- K^\pm$ contributions
 - 463 – a Coulomb-only curve, with the help of Appendix C, for other pairs including the Coulomb
464 interaction
- 465 3. The residual contributions to the ΛK correlation function is found by running each parent correla-
466 tion function through the appropriate transform matrix, via Eq.16
- 467 4. The primary and residual correlations are combined, via Eq.15 with Tab. A.1, to form $C'_{Fit}(k_{\text{True}}^*)$
- 468 5. The correlation function is corrected to account for momentum resolution effects using Eq. 19, to
469 obtain $C'_{Fit}(k_{\text{Rec}}^*)$
- 470 6. Finally, the non-flat background correction, $F_{\text{Bgd}}(k_{\text{Rec}}^*)$ is applied, and the final fit function is ob-
471 tained, $C_{\text{Fit}}(k_{\text{Rec}}^*) = C'_{\text{Fit}}(k_{\text{Rec}}^*) * F_{\text{Bgd}}(k_{\text{Rec}}^*)$

472 3.7 Systematic uncertainties

473 In order to understand the systematic uncertainties of our data, the analysis code was run many times
474 using slightly different values for a number of important cuts, and the results were compared. To quantify
475 the systematic errors on the data, all correlation functions built using all varied cut values were bin-by-
476 bin averaged, and the resulting variance of each bin was taken as the systematic error. The cuts included
477 in the systematic study, as well as the values used in the variations, are shown in Tab. 4 (ΛK_S^0) and Tab.
478 5 (ΛK^\pm). Note, the central value corresponds to that used in the analysis.

479 Similarly, the fit parameters extracted from all of these correlation functions were averaged, and the
480 resulting variances were taken as the systematic errors for the fit parameters. As with the systematic
481 errors on the data, this was performed for all varied cut values. Additionally, a systematic analysis
482 was done on our fit method through varying our k^* fit range, as well as varying our modeling of the
483 non-femtoscopic background. Our choice of k^* fit range was varied by $\pm 25\%$. As previously stated,
484 the non-femtoscopic backgrounds are modeled using the THERMINATOR 2 simulation for the ΛK^\pm
485 analyses, and with a linear form for the ΛK_S^0 system. To study the contribution of this choice to our
486 systematic errors, we modeled the backgrounds of all of our systems by fitting to the data with a with a
487 linear, quadratic, and Gaussian form. Additionally, we modeled the backgrounds of all systems with a
488 polynomial fit to the THERMINATOR simulation, scaled to match the data. The resulting uncertainties
489 in the extracted parameter sets were combined with our uncertainties arising from our particle and pair
490 cuts.

491 4 Results

492 Figure 5 shows our ΛK data with fits for all studied centrality bins (0-10%, 10-30%, and 30-50%). All
493 analyses were fit simultaneously across all centralities, with a single radius and normalization λ param-
494 eter for each centrality bin. Scattering parameters ($\Re f_0$, $\Im f_0$, d_0) were shared between pair-conjugate
495 systems, but assumed unique between the different ΛK charge combinations (i.e. a parameter set de-
496 scribing the ΛK^+ & $\bar{\Lambda} K^-$ system, a second set describing the ΛK^- & $\bar{\Lambda} K^+$ system, and a third for the
497 ΛK_S^0 & $\bar{\Lambda} K_S^0$ system). Each correlation function received a unique normalization parameter. The fits
498 were corrected for finite momentum resolution effects, non-femtoscopic backgrounds, and residual cor-
499 relations resulting from the feed-down from resonances. In Fig. 5, lines represent statistical errors, while
500 boxes represent systematic errors. The black solid curve shows the primary (ΛK) contribution to the fit,

ΛK_S^0 systematics

ΛK_S^0 systematics	
DCA $\Lambda(\bar{\Lambda})$	4, 5, 6 mm
DCA K_S^0	2, 3, 4 mm
DCA $\Lambda(\bar{\Lambda})$ Daughters	3, 4, 5 mm
DCA K_S^0 Daughters	2, 3, 4 mm
$\Lambda(\bar{\Lambda})$ Cosine of Pointing Angle	0.9992, 0.9993, 0.9994
K_S^0 Cosine of Pointing Angle	0.9992, 0.9993, 0.9994
DCA to Primary Vertex of $p(\bar{p})$ Daughter of $\Lambda(\bar{\Lambda})$	0.5, 1, 2 mm
DCA to Primary Vertex of $\pi^-(\pi^+)$ Daughter of $\Lambda(\bar{\Lambda})$	2, 3, 4 mm
DCA to Primary Vertex of π^+ Daughter of K_S^0	2, 3, 4 mm
DCA to Primary Vertex of π^- Daughter of K_S^0	2, 3, 4 mm
Average Separation of Like-Charge Daughters	5, 6, 7 cm

Table 4: ΛK_S^0 systematics ΛK^\pm systematics

ΛK^\pm systematics	
DCA $\Lambda(\bar{\Lambda})$	4, 5, 6 mm
DCA $\Lambda(\bar{\Lambda})$ Daughters	3, 4, 5 mm
$\Lambda(\bar{\Lambda})$ Cosine of Pointing Angle	0.9992, 0.9993, 0.9994
DCA to Primary Vertex of $p(\bar{p})$ Daughter of $\Lambda(\bar{\Lambda})$	0.5, 1, 2 mm
DCA to Primary Vertex of $\pi^-(\pi^+)$ Daughter of $\Lambda(\bar{\Lambda})$	2, 3, 4 mm
Average Separation of $\Lambda(\bar{\Lambda})$ Daughter with Same Charge as K^\pm	7, 8, 9 cm
Max. DCA to Primary Vertex in Transverse Plane of K^\pm	1.92, 2.4, 2.88
Max. DCA to Primary Vertex in Longitudinal Direction of K^\pm	2.4, 3.0, 3.6

Table 5: ΛK^\pm systematics

501 the green curve shows the fit to the non-femtoscopic background, and the purple curve shows the final
 502 fit after all corrections have been applied. The extracted fit values with uncertainties are printed as (fit
 503 value) \pm (statistical uncertainty) \pm (systematic uncertainty).

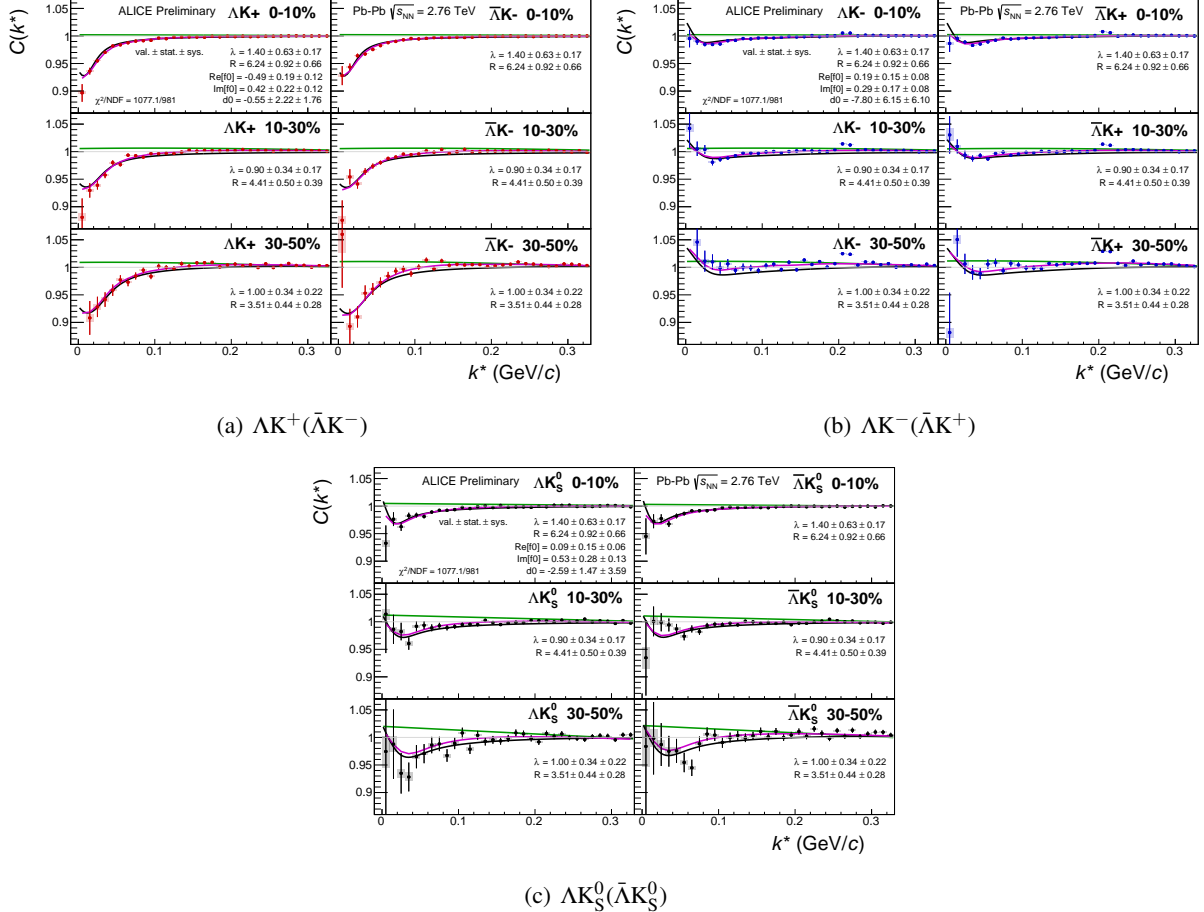


Fig. 5: Fits, with 3 residual correlations included, for all ΛK analyses across all studied centralities (0-10%, 10-30%, and 30-50%). The lines represent the statistical errors, while the boxes represent the systematic errors. The black solid line represents the primary (ΛK) correlation's contribution to the fit. The green line shows the fit to the non-flat background. The purple points show the fit after all residuals' contributions have been included, and momentum resolution and non-flat background corrections have been applied. The extracted fit values with uncertainties are printed.

504 Figure 6 summarizes well our results. In the summary plot, we show the extracted scattering parameters
 505 in the form of a $\Im(f_0)$ vs $\Re(f_0)$ plot, which includes the d_0 values to the right side. We also show the λ
 506 vs. radius parameters for all three of our studied centrality bins. In addition to our results, we show
 507 theoretical predictions made using chiral perturbation theory [19, 20].

508 We extract positive imaginary parts, $\Im(f_0)$, of the scattering lengths for all systems. We expect this,
 509 as $\Im(f_0)$ describes the inelastic scattering channels. More interestingly, our results show that the ΛK^+
 510 and ΛK^- systems differ in the sign of the real part, $\Re(f_0)$, of their scattering lengths (negative for
 511 ΛK^+ , and positive for ΛK^-). Furthermore, each of the three systems has a $\Re(f_0)$ unique from the
 512 others. The real part of the scattering length describes the effect of the strong interaction, making the
 513 difference in these systems quite intriguing. A positive $\Re(f_0)$ signifies that the effect of the strong force
 514 is attractive, which a negative $\Re(f_0)$ signifies a repulsion. We suggest that this difference could be due to
 515 an effect arising from different quark-antiquark interactions between the pairs ($s\bar{s}$ in ΛK^+ , $u\bar{u}$ in ΛK^-).
 516 An alternative explanation could be that the effect is due to the different net strangeness for each system.

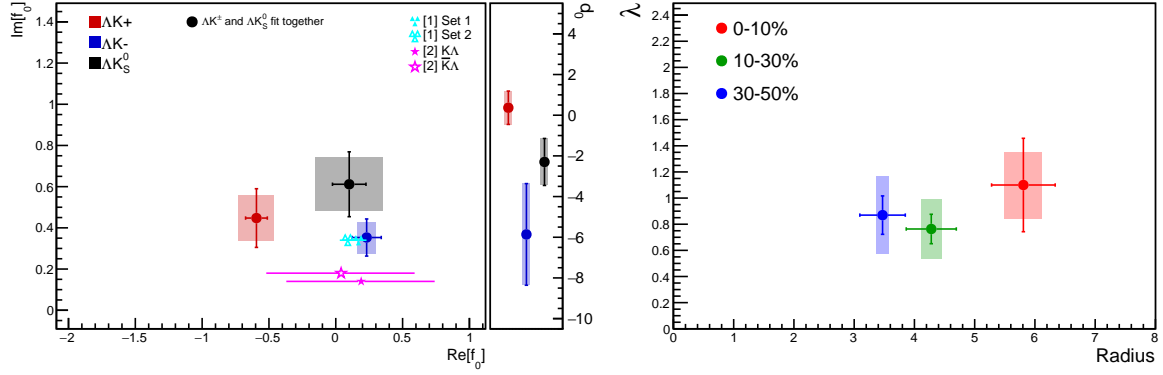


Fig. 6: Extracted scattering parameters for all of our ΛK systems. [Left]: $\Im(f_0)$ vs. $\Re(f_0)$, together with d_0 to the right. [Right]: λ vs. Radius for the studied centrality bins (0-10%, 10-30%, 30-50%). The green [19] and yellow [20] points show theoretical predictions made using chiral perturbation theory.

517 More specifically, systems with less net strangeness have more channels into which they can decay,
 518 causing a scarcity of pairs, i.e. a greater suppression of the correlation function, at low- k^* . However, an
 519 effect such as this really should instead manifest itself in $\Im(f_0)$ not $\Re(f_0)$. In any case, this remains a
 520 very interesting effect which needs an explanation.

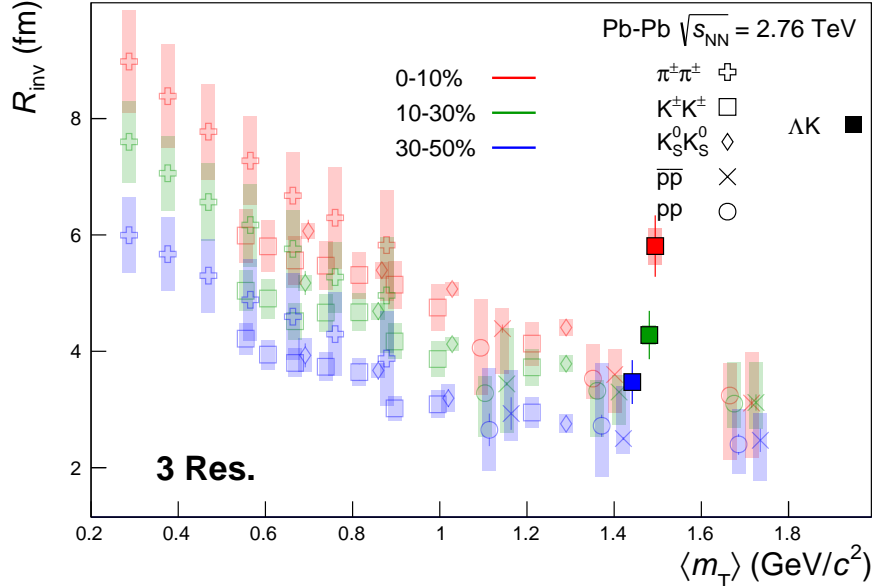


Fig. 7: 3 residual correlations in AK fits. Extracted fit R_{inv} parameters as a function of pair transverse mass (m_T) for various pair systems over several centralities. The ALICE published data [2] is shown with transparent, open symbols.

521 A comparison of our extracted radii to those of other systems measured by ALICE [2] is shown in Figure
 522 7. The figure shows extracted R_{inv} vs. m_T for several centralities and for several different systems. The
 523 radii are observed to increase for more central events, as expected from a simple geometric picture of the
 524 collisions. They also demonstrate a decreasing size with increasing m_T , as expected in the presence of
 525 collective radial flow [3]. It was found that [4], even in the presence of good global m_T -scaling for the
 526 three-dimensional radii in the LCMS frame, a particle species dependence will exist for the R_{inv} measured
 527 in the PRF, due to trivial kinematic reasons. These kinematic effects, resulting from the transformation
 528 from LCMS to PRF, causes smaller masses to exhibit larger R_{inv} [2] (explaining, for instance, how the
 529 pion radii are systematically higher than kaon radii at the same approximate m_T).

It is clear from the results that the ΛK systems do not conform to the approximate m_T -scaling of the pair source sizes.¹ At first thought, this may appear to be a troubling result; the approximate scaling is an observed consequence of the collective behavior of the soft (low- p_T) sector of the produced system. The Λ and K particles certainly participate in the collective expansion of the QGP medium, but, importantly, they are non-identical particles. Taking a closer look at Fig. 7, one can see that the previously published data (transparent points), and the established (approximate) m_T -scaling trend, are for identical particle analyses only. When dealing with non-identical particles, the pair emission source, which is measured by femtoscopy, is the superposition of two single-particle sources. In general, each single-particle source will have its own size, shape, and space-time position within the produced medium, which is unique from its paired partner. The hydrodynamic nature of the medium produces the approximate m_T -scaling with respect to these single-particle sources, not the pair sources. The combination of two unique sources separated in space-time, when probing correlations between non-identical particle pairs, leads to extracted radii falling outside of the (identical particle femtoscopy) m_T -scaling trend.

It is well established that non-identical particle femtoscopic studies are able to probe deeper than the second moments of the pair distribution functions accessed via identical particle studies. In addition to this, non-identical particle studies are able to measure the relative emission shifts, the first moments of the emission function. For the study of ΛK pairs at mid-rapidity in Pb-Pb collisions, we expect a separation of the single-particle sources in the out direction. One elegant method for extracting information about the emission asymmetries is via a spherical decomposition of the correlation function. With this method, one can draw a wealth of information from just a few components of the decomposition. Particularly, the C_{00} component is similar to the 1D correlation functions typically studied, and probes the overall size of the source. The $\Re C_{11}$ component probes the asymmetry of the system in the out direction; a non-zero value reveals the asymmetry. Figure D.1 in App. D shows the C_{00} and $\Re C_{11}$ components of the spherical decomposition of our ΛK^+ data in the 0-10% centrality bin. The $\Re C_{11}$ component shows a clear deviation from zero, and the negative value signifies that the Λ particles are, on average, emitted further out and/or earlier than the K mesons. This effect is supported by the results obtained from the THERMINATOR 2 model, shown in Fig. E.1. The effect of a non-zero shift in the source will naturally lead to larger measured radii. This is intuitive, and also reaffirmed in our simulation with THERMINATOR 2 shown in App. E. We have also shown larger effective radii to result from inserting a Gaussian source with a non-zero shift into the Koonin-Pratt equation and numerically integrating.

5 Summary

Results from a femtoscopic analysis of ΛK correlations in Pb-Pb collisions at $\sqrt{s_{NN}} = 2.76$ TeV with ALICE at the LHC have been presented. The femtoscopic radii, λ parameters, and scattering parameters were extracted from one-dimensional correlation functions in terms of the invariant momentum difference. The scattering parameters of ΛK pairs in all three charge combinations (ΛK^+ , ΛK^- , and ΛK_S^0) have been measured for the first time. We observe a striking difference in the ΛK^+ and ΛK^- correlation functions, which is reflected in the unique set of scattering parameters extracted for each. The ΛK^+ systems exhibits a negative $\Re(f_0)$, while that extracted from the ΛK^- system is positive. The physics underlying this phenomenon is currently not well understood, but we suggest this could be due

¹ For our non-identical particle pairs, to be more directly analogous to the single particle m_T , we define the pair transverse mass as

$$\begin{aligned} m_{T,pair}^2 &= \left(\frac{m_{inv}}{2}\right)^2 + \left(\frac{1}{2}|p_{T,1} + p_{T,2}|\right)^2 \\ &= (K^0)^2 - (K^3)^2 \\ \text{where } K^\mu &\equiv \frac{1}{2}(p_1^\mu + p_2^\mu) \end{aligned}$$

569 to different quark-antiquark interactions between the pairs, or from different net strangeness for each
 570 system. Finally, we find that the Λ K systems exhibit source radii larger than expected from extrapolation
 571 from identical particle femtoscopic studies. We understand this effect to result from the separation in
 572 space-time of the single-particle Λ and K source distributions.

573 **Acknowledgements**

574 **References**

- 575 [1] M. A. Lisa, S. Pratt, R. Soltz, and U. Wiedemann, “Femtoscopy in relativistic heavy ion
 576 collisions,” *Ann. Rev. Nucl. Part. Sci.* **55** (2005) 357–402, [arXiv:nucl-ex/0505014](https://arxiv.org/abs/nucl-ex/0505014)
 577 [nucl-ex].
- 578 [2] ALICE Collaboration, J. Adam *et al.*, “One-dimensional pion, kaon, and proton femtoscopy in
 579 Pb-Pb collisions at $\sqrt{s_{NN}} = 2.76$ TeV,” *Phys. Rev.* **C92** no. 5, (2015) 054908, [arXiv:1506.07884](https://arxiv.org/abs/1506.07884)
 580 [nucl-ex].
- 581 [3] S. V. Akkelin and Yu. M. Sinyukov, “The HBT interferometry of expanding sources,” *Phys. Lett.*
 582 **B356** (1995) 525–530.
- 583 [4] A. Kisiel, M. Gaayn, and P. Boek, “Pion, kaon, and proton femtoscopy in Pb-Pb collisions at
 584 $\sqrt{s_{NN}} = 2.76$ TeV modeled in (3+1)D hydrodynamics,” *Phys. Rev.* **C90** no. 6, (2014) 064914,
 585 [arXiv:1409.4571](https://arxiv.org/abs/1409.4571) [nucl-th].
- 586 [5] R. Lednický and V. L. Lyuboshitz *Sov. J. Nucl. Phys.* **35** (1982) 770.
- 587 [6] ALICE Collaboration, K. Aamodt *et al.*, “The alice experiment at the cern lhc,” *JINST* **3** (2008)
 588 S08002. <http://stacks.iop.org/1748-0221/3/i=08/a=S08002>.
- 589 [7] ALICE Collaboration, B. Abelev *et al.*, “Centrality determination of Pb-Pb collisions at $\sqrt{s_{NN}} =$
 590 2.76 TeV with ALICE,” *Phys. Rev.* **C88** no. 4, (2013) 044909, [arXiv:1301.4361](https://arxiv.org/abs/1301.4361) [nucl-ex].
- 591 [8] J. Alme *et al.*, “The ALICE TPC, a large 3-dimensional tracking device with fast readout for
 592 ultra-high multiplicity events,” *Nucl. Instrum. Meth. A* **622** (2010) 316–367, [arXiv:1001.1950](https://arxiv.org/abs/1001.1950)
 593 [physics.ins-det].
- 594 [9] ALICE Collaboration, B. B. Abelev *et al.*, “Performance of the ALICE Experiment at the CERN
 595 LHC,” *Int. J. Mod. Phys. A* **29** (2014) 1430044, [arXiv:1402.4476](https://arxiv.org/abs/1402.4476) [nucl-ex].
- 596 [10] A. Akindinov *et al.*, “Performance of the ALICE Time-Of-Flight detector at the LHC,” *Eur. Phys.
 597 J. Plus* **128** (2013) 44.
- 598 [11] X.-N. Wang and M. Gyulassy, “hijing: A Monte Carlo model for multiple jet production in pp,
 599 pA, and AA collisions,” *Phys. Rev. D* **44** (Dec, 1991) 3501–3516.
 600 <https://link.aps.org/doi/10.1103/PhysRevD.44.3501>.
- 601 [12] R. Brun, F. Bruyant, F. Carminati, S. Giani, M. Maire, A. McPherson, G. Patrick, and L. Urban,
 602 “GEANT Detector Description and Simulation Tool.”
- 603 [13] **Particle Data Group** Collaboration, C. Patrignani *et al.*, “Review of Particle Physics,” *Chin.
 604 Phys.* **C40** no. 10, (2016) 100001.
- 605 [14] S. E. Koonin, “Proton Pictures of High-Energy Nuclear Collisions,” *Phys. Lett.* **B70** (1977) 43–47.
- 606 [15] S. Pratt, T. Csorgo, and J. Zimanyi, “Detailed predictions for two pion correlations in
 607 ultrarelativistic heavy ion collisions,” *Phys. Rev.* **C42** (1990) 2646–2652.

- 608 [16] A. Kisiel, H. Zbroszczyk, and M. Szymaski, “Extracting baryon-antibaryon strong interaction
609 potentials from p $\bar{\Lambda}$ femtoscopic correlation functions,” *Phys. Rev.* **C89** no. 5, (2014) 054916,
610 arXiv:1403.0433 [nucl-th].
- 611 [17] M. Chojnacki, A. Kisiel, W. Florkowski, and W. Broniowski, “THERMINATOR 2: THERMal
612 heavy IoN generATOR 2,” *Comput. Phys. Commun.* **183** (2012) 746–773, arXiv:1102.0273
613 [nucl-th].
- 614 [18] A. Kisiel, “Non-identical particle correlation analysis in the presence of non-femtoscopic
615 correlations,” *Acta Physica Polonica B* **48** (04, 2017) 717.
- 616 [19] Y.-R. Liu and S.-L. Zhu, “Meson-baryon scattering lengths in HB chi PT,” *Phys. Rev.* **D75** (2007)
617 034003, arXiv:hep-ph/0607100 [hep-ph].
- 618 [20] M. Mai, P. C. Bruns, B. Kubis, and U.-G. Meissner, “Aspects of meson-baryon scattering in three
619 and two-flavor chiral perturbation theory,” *Phys. Rev.* **D80** (2009) 094006, arXiv:0905.2810
620 [hep-ph].
- 621 [21] A. Stavinskiy *et al.*, “Some new aspects of femtoscopy at high energy,” *Nukleonika* **49**
622 (**Supplement 2**) (2004) S23.
- 623 [22] R. Lednický, “Finite-size effects on two-particle production in continuous and discrete spectrum,”
624 *Phys. Part. Nucl.* **40** (2009) 307–352, arXiv:nucl-th/0501065 [nucl-th].

625 **A λ Parameters**

AK ⁺ residuals		$\bar{A}K^-$ residuals		AK ⁻ residuals		$\bar{A}K^+$ residuals		AK _S ⁰ residuals		$\bar{A}K_S^0$ residuals	
Pair System	λ value	Pair System	λ value	Pair System	λ value	Pair System	λ value	Pair System	λ value	Pair System	λ value
3 Residuals (Max Parent $c\tau_{\text{decay}} = 10 \text{ fm}$)											
AK ⁺	0.527	$\bar{A}K^-$	0.526	AK ⁻	0.526	$\bar{A}K^+$	0.527	AK _S ⁰	0.543	$\bar{A}K_S^0$	0.544
$\Sigma^0 K^+$	0.111	$\bar{\Sigma}^0 K^-$	0.110	$\Sigma^0 K^-$	0.110	$\bar{\Sigma}^0 K^+$	0.111	$\Sigma^0 K_S^0$	0.120	$\bar{\Sigma}^0 K_S^0$	0.120
$\Xi^0 K^+$	0.039	$\bar{\Xi}^0 K^-$	0.035	$\Xi^0 K^-$	0.038	$\bar{\Xi}^0 K^+$	0.036	$\Xi^0 K_S^0$	0.042	$\bar{\Xi}^0 K_S^0$	0.039
$\Xi^- K^+$	0.050	$\bar{\Xi}^+ K^-$	0.046	$\Xi^- K^-$	0.050	$\bar{\Xi}^+ K^+$	0.046	$\Xi^- K_S^0$	0.054	$\bar{\Xi}^+ K_S^0$	0.050
Other	0.226	Other	0.235	Other	0.228	Other	0.233	Other	0.194	Other	0.199
Fakes	0.048	Fakes	0.048	Fakes	0.048	Fakes	0.048	Fakes	0.048	Fakes	0.048
10 Residuals (Max Parent $c\tau_{\text{decay}} = 4 \text{ fm}$)											
AK ⁺	0.180	$\bar{A}K^-$	0.180	AK ⁻	0.179	$\bar{A}K^+$	0.181	AK _S ⁰	0.192	$\bar{A}K_S^0$	0.193
$\Sigma^0 K^+$	0.116	$\bar{\Sigma}^0 K^-$	0.114	$\Sigma^0 K^-$	0.115	$\bar{\Sigma}^0 K^+$	0.116	$\Sigma^0 K_S^0$	0.125	$\bar{\Sigma}^0 K_S^0$	0.124
$\Xi^0 K^+$	0.040	$\bar{\Xi}^0 K^-$	0.037	$\Xi^0 K^-$	0.040	$\bar{\Xi}^0 K^+$	0.037	$\Xi^0 K_S^0$	0.043	$\bar{\Xi}^0 K_S^0$	0.040
$\Xi^- K^+$	0.052	$\bar{\Xi}^+ K^-$	0.047	$\Xi^- K^-$	0.052	$\bar{\Xi}^+ K^+$	0.048	$\Xi^- K_S^0$	0.056	$\bar{\Xi}^+ K_S^0$	0.052
$\Sigma^{*+} K^+$	0.054	$\bar{\Sigma}^{*-} K^-$	0.051	$\Sigma^{*+} K^-$	0.053	$\bar{\Sigma}^{*-} K^+$	0.051	$\Sigma^{*+} K_S^0$	0.058	$\bar{\Sigma}^{*-} K_S^0$	0.055
$\Sigma^{*-} K^+$	0.048	$\bar{\Sigma}^{*+} K^-$	0.050	$\Sigma^{*-} K^-$	0.048	$\bar{\Sigma}^{*+} K^+$	0.050	$\Sigma^{*-} K_S^0$	0.052	$\bar{\Sigma}^{*+} K_S^0$	0.054
$\Sigma^{*0} K^+$	0.048	$\bar{\Sigma}^{*0} K^-$	0.045	$\Sigma^{*0} K^-$	0.048	$\bar{\Sigma}^{*0} K^+$	0.045	$\Sigma^{*0} K_S^0$	0.052	$\bar{\Sigma}^{*0} K_S^0$	0.048
ΛK^{*0}	0.046	$\bar{\Lambda} \bar{K}^{*0}$	0.047	$\Lambda \bar{K}^{*0}$	0.046	$\bar{\Lambda} K^{*0}$	0.047	ΛK^{*0}	0.022	$\bar{\Lambda} K^{*0}$	0.022
$\Sigma^0 K^{*0}$	0.041	$\bar{\Sigma}^0 \bar{K}^{*0}$	0.041	$\Sigma^0 \bar{K}^{*0}$	0.041	$\bar{\Sigma}^0 K^{*0}$	0.041	$\Sigma^0 K^{*0}$	0.019	$\bar{\Sigma}^0 K^{*0}$	0.019
$\Xi^0 K^{*0}$	0.014	$\bar{\Xi}^0 \bar{K}^{*0}$	0.013	$\Xi^0 \bar{K}^{*0}$	0.014	$\bar{\Xi}^0 K^{*0}$	0.013	$\Xi^0 K^{*0}$	0.007	$\bar{\Xi}^0 K^{*0}$	0.006
$\Xi^- K^{*0}$	0.018	$\bar{\Xi}^+ \bar{K}^{*0}$	0.017	$\Xi^- \bar{K}^{*0}$	0.018	$\bar{\Xi}^+ K^{*0}$	0.017	$\Xi^- K^{*0}$	0.009	$\bar{\Xi}^+ K^{*0}$	0.008
Other	0.295	Other	0.310	Other	0.299	Other	0.307	Other	0.318	Other	0.330
Fakes	0.048	Fakes	0.048	Fakes	0.048	Fakes	0.048	Fakes	0.048	Fakes	0.048

Table A.1: λ values for the individual components of the AK correlation functions for the case of 3 and 10 residual contributions.

626 B Stavinskiy Reference Method

627 Another option for obtaining the reference distribution, $B(k^*)$, is to use, what we will refer to as, the
 628 “Stavinskiy method” [21]. The method was first proposed to handle the case of one event femtoscopy, and
 629 has been suggested for use in eliminating momentum conservation effects in the reference distribution
 630 [1]. The method is appropriate for collisions between symmetric projectiles, at sufficiently large energy,
 631 with a detector which is symmetrical with respect to the transition $\mathbf{r} \rightarrow -\mathbf{r}$. The purpose of our use
 632 of the Stavinskiy method is to rid the correlation functions of the non-femtoscopic background. More
 633 specifically, our intent is to handle background contributions from elliptic flow, and other sources having
 634 reflection symmetry in the transverse plane. With the Stavinskiy method, mixed-event pairs are not used
 635 for the reference distribution; instead, same-event pseudo-pairs, formed by rotating one particle in a real
 636 pair by 180° in the transverse plane, are used. This rotation rids the pairs of any femtoscopic correlation,
 637 while maintaining correlations due to elliptic flow (and other suitably symmetric contributors).

638 The results of correctly implementing such a procedure are shown in Figure B.1. The figure shows
 639 the Stavinskiy method does a very good job of ridding the ΛK^\pm correlations of their non-femtoscopic
 640 backgrounds. We also see the procedure does not work as well on the ΛK_S^0 system.

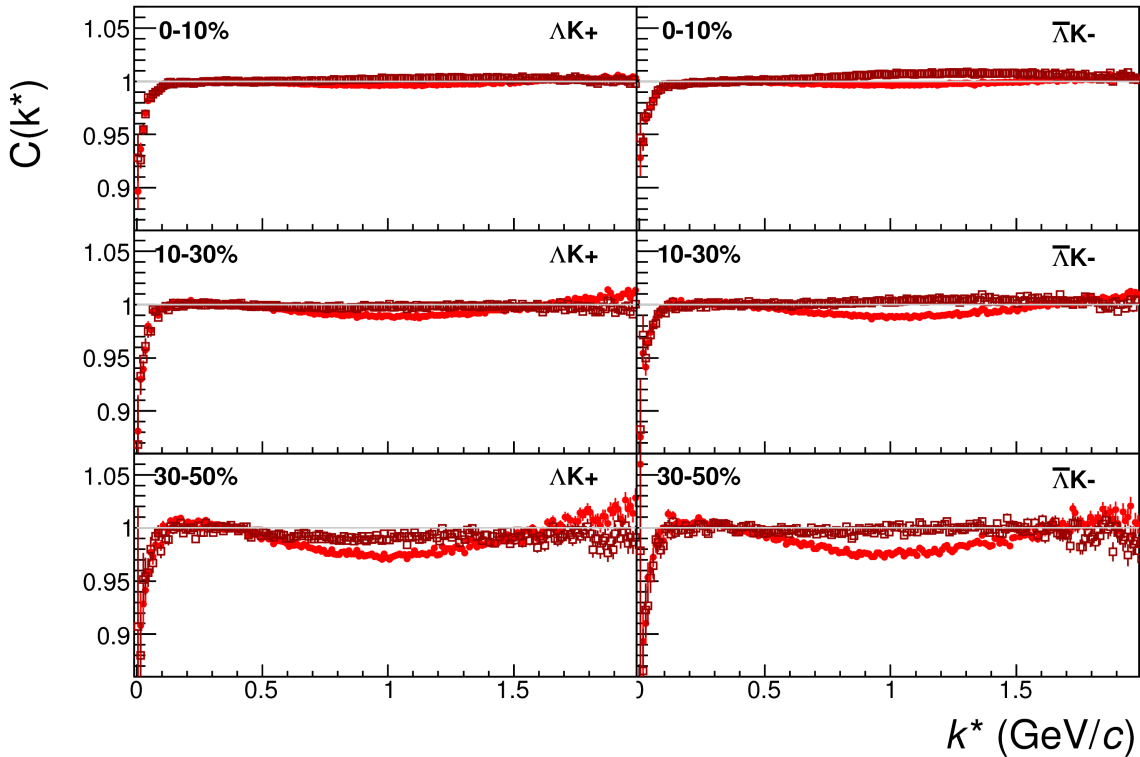


Fig. B.1: $\Lambda K^+(\bar{\Lambda} K^-)$ correlation functions built using the Stavinskiy method for 0-10%, 10-30%, and 30-50% centralities. Closed symbols represent correlations built using the normal mixed-event reference distribution, while open symbols represent correlations formed using the Stavinskiy same-event pseudo-pairs as a reference.

641 Now, one must be somewhat careful when applying this Stavinskiy method. We found that, in order to
 642 obtain correct results, we had to run our pseudo-pairs through the same pair cuts used in our analyses. In
 643 an ideal world, our pair cut would only remove truly bad pairs from splitting, merging, etc. In the
 644 real world, the pair cut always throws out some of the good with the bad. For the pseudo-pairs to form a
 645 reliable reference, they too must experience the pair cut, and the loss of “good” pseudo-pairs. We found
 646 this issue affected mainly our ΛK^+ & $\bar{\Lambda} K^-$ analysis.

647 C Strong and Coulomb Fitter

648 When modeling systems which include both strong and Coulomb effects, Eq. 10 is no longer valid, and,
 649 in fact, there is no analytical form with which to fit. To solve such a problem, and to fit such a system, one
 650 must develop a more fundamental model, beginning with Eq. 4 and using the two-particle wave-function
 651 including both strong and Coulomb interactions [22]:

$$\Psi_{\mathbf{k}^*}(\mathbf{r}^*) = e^{i\delta_c} \sqrt{A_c(\eta)} [e^{i\mathbf{k}^*\cdot\mathbf{r}^*} F(-i\eta, 1, i\xi) + f_c(k^*) \frac{\tilde{G}(\rho, \eta)}{r^*}] \quad (\text{C.1})$$

652 where $\rho = k^* r^*$, $\eta = (k^* a_c)^{-1}$, $\xi = \mathbf{k}^* \cdot \mathbf{r}^* + k^* r^* \equiv \rho(1 + \cos \theta^*)$, and $a_c = (\mu z_1 z_2 e^2)^{-1}$ is the two-
 653 particle Bohr radius (including the sign of the interaction). δ_c is the Coulomb s-wave phase shift, $A_c(\eta)$
 654 is the Coulomb penetration factor, $\tilde{G} = \sqrt{A_c}(G_0 + iF_0)$ is a combination of the regular (F_0) and singular
 655 (G_0) s-wave Coulomb functions. $f_c(k^*)$ is the s-wave scattering amplitude:

$$f_c(k^*) = [\frac{1}{f_0} + \frac{1}{2} d_0 k^{*2} - \frac{2}{a_c} h(\eta) - ik^* A_c(\eta)]^{-1} \quad (\text{C.2})$$

656 where, the “h-function”, $h(\eta)$, is expressed through the digamma function, $\psi(z) = \Gamma'(z)/\Gamma(z)$ as:

$$h(\eta) = 0.5[\psi(i\eta) + \psi(-i\eta) - \ln(\eta^2)] \quad (\text{C.3})$$

657 In this case, the λ parameter may be included as:

$$C(\mathbf{k}^*) = (1 - \lambda) + \lambda \int S(\mathbf{r}^*) |\Psi_{\mathbf{k}^*}^S(\mathbf{r}^*)|^2 d^3 \mathbf{r}^* \quad (\text{C.4})$$

658 To build a fit function for a system including both strong and Coulomb interactions we considered two
 659 related options. The first option was to numerically integrate Eq.4. The second option was to simulate
 660 a large sample of particle pairs, calculate the wave function describing the interaction, and average to
 661 obtain the integral in Eq.4. In either case, the solution would involve some very complicated mathemat-
 662 ical functions, as can be seen in Eqs. C.1 to C.3. Having no experience with either of these options, we
 663 elected the latter of simulating pairs.

664 D Spherical Harmonic Decomposition

665 In Fig. D.1 we show results for the C_{00} and $\Re C_{11}$ components from the spherical decomposition of our
 666 ΛK^+ system in the 0-10% centrality bin. As seen in the figure, the C_{00} signal is similar to that observed
 667 in our one-dimensional study. The $\Re C_{11}$ component shows a clear deviation from zero, and the negative
 668 value signifies that the Λ particles are, on average, emitted further out and/or earlier than the K mesons.

669 E Relative Emission Shifts with THERMINATOR 2

670 Fig. E.1 shows results from the THERMINATOR 2 event generator for an impact parameter of $b = 2$ fm.
 671 As THERMINATOR does not include any final state effects, the femtoscopic correlation was introduced
 672 by assuming a set of scattering parameters $(\Re f_0, \Im f_0, d_0) = (-1.16, 0.51, 1.08)$ and weighting the signal
 673 distribution (numerator pairs) with the modulus squared of the two-particle wave function, $|\Psi|^2$.

674 The top left of Fig. E.1(a) shows a fit to the one-dimensional correlation function from THERMINA-
 675 TOR 2. The scattering parameters are known precisely here, as they served as the weights used in the
 676 simulation, and are kept constant in the fit. We are interested in looking at the extracted one-dimensional

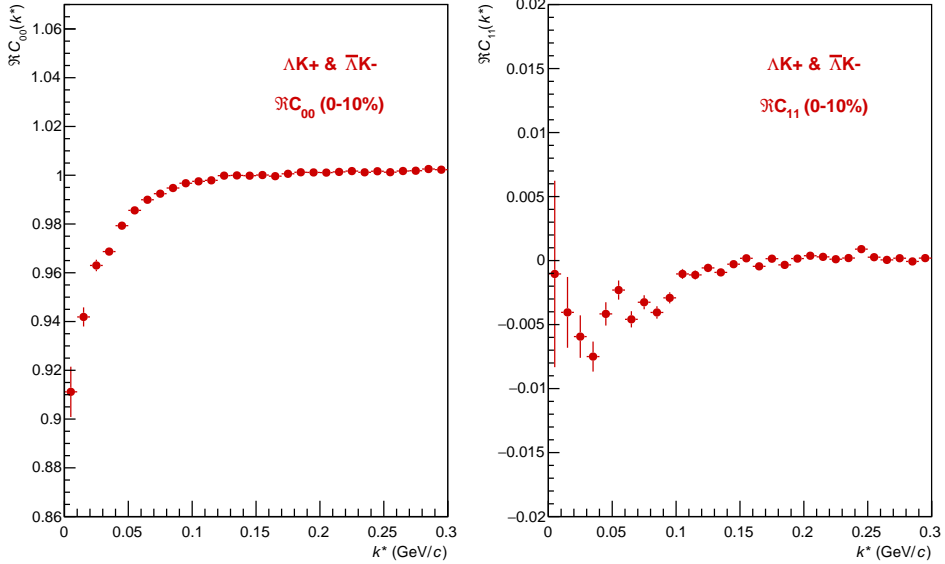
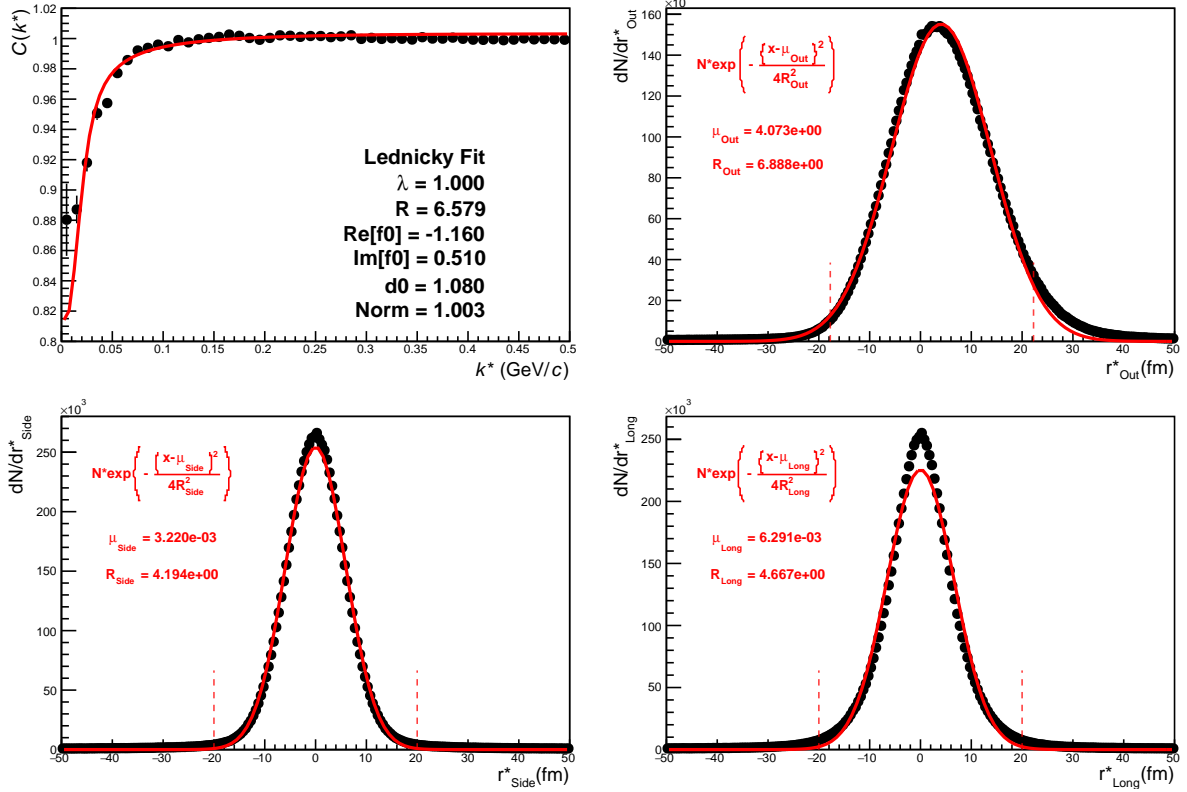


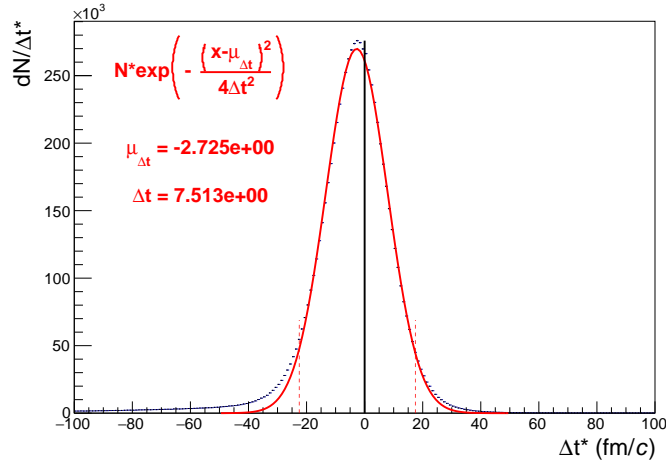
Fig. D.1: C_{00} (left) and $\Re C_{11}$ (right) components of a spherical harmonic decomposition of the ΛK^+ correlation function for the 0-10% centrality bin. The C_{00} component is similar to the 1D correlation functions typically studied, and probes the overall size of the source. The $\Re C_{11}$ component probes the asymmetry in the system; a non-zero value reveals the asymmetry

677 source size here, so the λ parameter is also fixed at unity. The other three plots in Fig. E.1(a) show the
 678 source distribution in the out (top right), side (bottom left), and long (bottom right) directions (all in the
 679 PRF). The source distributions have all been fitted with a Gaussian form, the result of which is printed
 680 within the respective plot. One immediately sees a significant shift in the out direction, $\mu_{\text{out}} \approx 4$ fm, and
 681 negligible shift in the other two directions, $\mu_{\text{side}} \approx \mu_{\text{long}} \approx 0$ fm. The figure demonstrates that, within
 682 the THERMINATOR 2 model, the Λ is, on average, emitted further out than its K partner. Finally, Fig.
 683 E.1(b) shows the distribution of the relative time of emittance, again in the PRF. The figure shows that
 684 the Λ is, on average, emitted earlier than its K partner.

685 We end this section with a brief look at how a spatial separation of the single particle sources affects
 686 the radii extracted from a femtoscopic analysis. To achieve this, we use THERMINATOR 2 in a similar
 687 fashion as described above, but with one important difference. Instead of taking the source information
 688 from THERMINATOR 2, we instead draw the source from a pre-determined Gaussian distribution. In
 689 all cases, we take $R_{\text{out}} = R_{\text{side}} = R_{\text{long}} = 5$ fm, and $\mu_{\text{side}} = \mu_{\text{long}} = 0$ fm. In Figure E.2, we show results
 690 for the case of $\mu_{\text{out}} = 1$ fm, $\mu_{\text{out}} = 3$ fm, and $\mu_{\text{out}} = 6$ fm. In this figure, we do not show the side and
 691 long distributions, as they are simple Gaussians of width 5 fm centered about the origin. The figure
 692 demonstrates that as the separation μ_{out} increases, so do the extracted femtoscopic radii.



(a) (Top Left) Simple fit on simulation from THERMINATOR 2. Generated source in the (Top Right) out, (Bottom Left) side, and (Bottom Right) long directions.



(b) Temporal characteristics of the source.

Fig. E.1: Extracted radius when performing a simple fit on simulation from THERMINATOR 2, along with the spatio-temporal characteristics generated by the simulation.

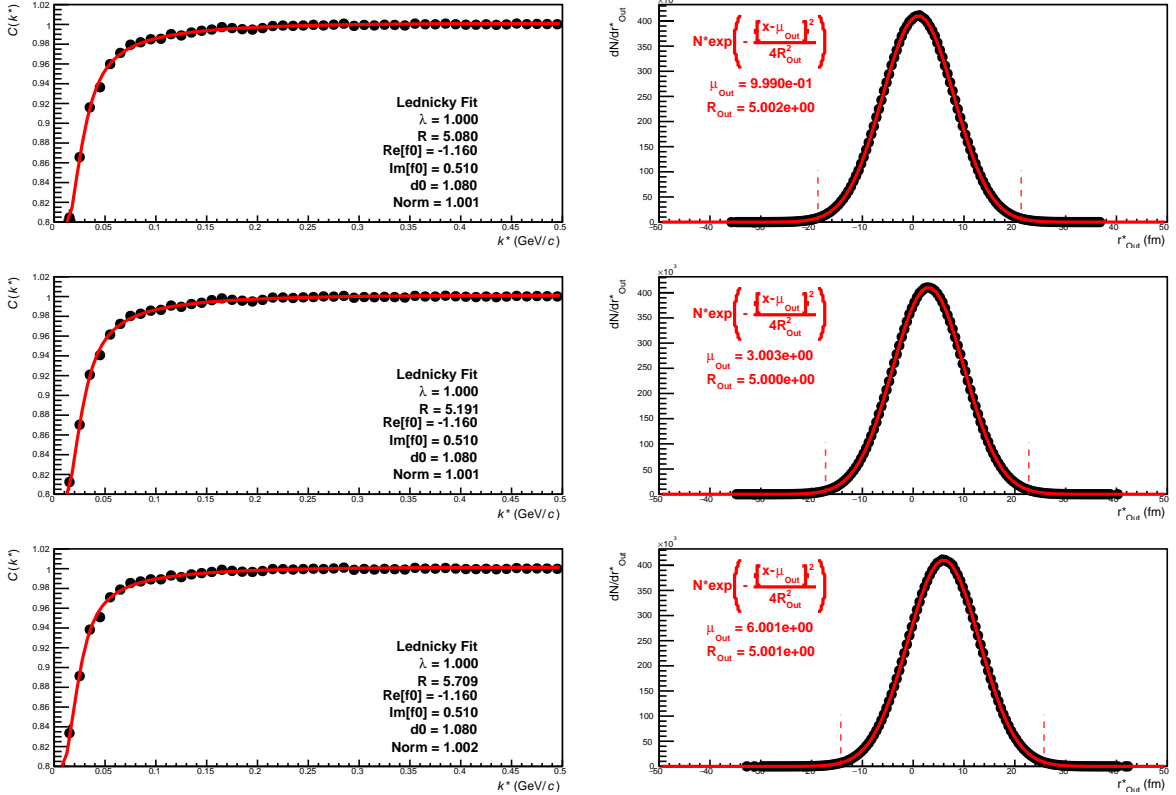


Fig. E.2: Probing the effect of varying the source shift in the outward direction, μ_{Out} , within the THERMINATOR 2 framework. To achieve this, we formed particle pairs from the simulation, but altered their spatial characteristics by drawing the out, side, and long components from pre-determined Gaussian distributions. The plots on the left show fits resulting from the sources (in the out direction) shown on the right. The sources in the side and long directions are not shown, and are both Gaussians of width 5 fm centered at the origin for all cases. Moving from top to bottom, μ_{Out} increase from 0 to 6 fm, the effect of which clearly increases the effective radius extracted in the fit.

693 **F The ALICE Collaboration**